nature physics

SUPPLEMENTARY INFORMATION

https://doi.org/10.1038/s41567-017-0040-5

In the format provided by the authors and unedited.

Rethinking pattern formation in reaction–diffusion systems

J. Halatek and E. Frey*

Arnold-Sommerfeld-Center for Theoretical Physics and Center for NanoScience, Department of Physics, Ludwig-Maximilians-Universität München, München, Germany. *e-mail: frey@lmu.de

Rethinking pattern formation in reaction–diffusion systems - Supplementary Document

J. Halatek and E. Frey*

Arnold Sommerfeld Center for Theoretical Physics and Center for NanoScience, Department of Physics, Ludwig-Maximilians-Universität München, Theresienstraße 37, D-80333 München, Germany

(Dated: December 4, 2017)

* frey@lmu.de

CONTENTS

I. TWO-COMPONENT REACTION-DIFFUSION MODEL

To illustrate our main ideas and to place our exposition in a sufficiently general framework, we consider the simplest possible reaction-diffusion system: a chemical system comprises two chemical components A and B confined to a finite one-dimensional domain of length L. Let $a(x,t)$ and $b(x,t)$ denote the local densities of components A and B, respectively. We are interested in dynamical systems that conserve the total mass $N = \int n_x(t)\,dx$, where $n_x(t) := a(x,t) + b(x,t)$ is the local value of the *total mass density*. Our goal in this supplementary section is to show that lateral instabilities generically induce mass redistribution and thereby shift local equilibria. The most general reaction-diffusion equation describing such a dynamics reads

$$\partial_t a = D_a \partial_x^2 a + f(a,b)\,, \tag{1a}$$

$$\partial_t b = D_b \partial_x^2 b - f(a,b)\,, \tag{1b}$$

where the function $f(a,b)$ accounts for all chemical reactions, and D_a and D_b are the diffusion constants of the chemical components A and B, respectively. The boundary conditions can be open, periodic, no-flux, or Dirichlet type.

A. Dynamics without diffusive coupling

For a *well-mixed system*, the dynamics reduces to

$$\partial_t a = f(a,b)\,, \tag{2a}$$

$$\partial_t b = -f(a,b)\,, \tag{2b}$$

with spatially uniform densities $a(t)$ and $b(t)$. The equilibria (fixed points) of the reactive dynamics, a^* and b^*, are given by the stationarity condition $f(a^*,b^*)=0$ supplemented by the mass conservation constraint $a^* + b^* = \bar{n}$, where $\bar{n} = N/L$ is the invariant total mass density. To study the *linear stability* of these equilibria one defines the displacement vector $\delta\boldsymbol{a} = \Big[a-a^*\ ,\ b-b^*\Big]^T$, and considers the linearised system corresponding to Eq. (2),

$$\partial_t\, \delta\boldsymbol{a} = \mathcal{J}\, \delta\boldsymbol{a}\,, \tag{3}$$

with the Jacobian given by

$$\mathcal{J} = \begin{bmatrix} f^a & f^b \\ -f^a & -f^b \end{bmatrix}, \tag{4}$$

where $f^a := \frac{\partial f}{\partial a}|_{(a^*,b^*)}$ and $f^b := \frac{\partial f}{\partial b}|_{(a^*,b^*)}$ are the first order Taylor coefficients evaluated at the fixed point (a^*,b^*). With the ansatz $\delta\boldsymbol{a}(t) = \mathrm{e}^{\sigma t}\,\boldsymbol{e}$ one finds the eigenvalues

$$\sigma^{(1)} = 0\,, \tag{5a}$$

$$\sigma^{(2)} = f^a - f^b\,, \tag{5b}$$

and the corresponding eigenvectors,

$$\boldsymbol{e}^{(1)} = \left[-f^b/f^a \ , \ 1\right]^T , \tag{6a}$$

$$\boldsymbol{e}^{(2)} = \left[-1 \ , \ 1\right]^T . \tag{6b}$$

The first eigenpair defines a *center space*, where the eigenvector $\boldsymbol{e}^{(1)}$ is tangent to the line of fixed points given by $f(a,b)=0$, which explains why the associated eigenvalue $\sigma^{(1)}$ is zero. The second eigenpair defines the stability of the equilibrium (fixed point) against perturbations that preserve the total particle density $\bar{n}$; note that the eigenvector $\boldsymbol{e}^{(2)}$ spans a 1-simplex in phase space defined by the mass conservation constraint $a+b=\bar{n}$, whereas $\boldsymbol{e}^{(1)}$ breaks mass conservation (c.f. main text Fig. 1).

Before continuing with the stability analysis of these spatially uniform equilibria (a^*, b^*) against spatially non-uniform perturbations, we first study a particular system where the initial mass distribution is spatially non-uniform, $n_x(0)$, but there is no mass transport through diffusion. This is equivalent to the following 'Gedankenkonstrukt' (notional construct), whose significance for the spatiotemporal dynamics will become clear as we proceed: Imagine the one-dimensional system be divided up into a set of (infinitesimal) compartments (*reactors*) where each of them is considered as well-mixed but they are separated from each other by walls which inhibit any diffusive flux; for an illustration see main text Fig. 1a. Then, for a compartment at position x, we have the same well-mixed dynamics as above,

$$\partial_t a_x = f(a_x, b_x) , \tag{7a}$$

$$\partial_t b_x = -f(a_x, b_x) , \tag{7b}$$

but with the difference that each of these compartments contains a different amount of mass as specified by the local value of the total mass density $n_x(0)$. Since there is no diffusion we have $\partial_t n_x(t)=0$, i.e. the total mass density remains locally invariant in time: $n_x(t)=n_x(0)=:n_x$. As a consequence, each spatial position x is characterised by a different fixed point, (a_x^*, b_x^*), which we term *local equilibrium*. It is obtained from the conditions of local stationarity $f(a_x^*, b_x^*)=0$, and local mass conservation $a_x^*+b_x^*=n_x$. Upon defining the displacement vector $\delta\boldsymbol{a}_x(t)=\left[a_x(t)-a_x^* \ , \ b_x(t)-b_x^*\right]^T$, one can study the stability of these local equilibria. The linearised systems corresponding to Eq. (7a) reads

$$\partial_t \, \delta\boldsymbol{a} = \mathcal{J}_x \, \delta\boldsymbol{a} \tag{8}$$

with the local Jacobian given by

$$\mathcal{J}_x = \begin{bmatrix} f_x^a & f_x^b \\ -f_x^a & -f_x^b \end{bmatrix} , \tag{9}$$

where $f_x^a \equiv \frac{\partial f}{\partial a}|_{(a_x^*, b_x^*)}$ and $f_x^b \equiv \frac{\partial f}{\partial b}|_{(a_x^*, b_x^*)}$. For each space point x, the linear system, Eq.(8), is solved by the ansatz $\delta\boldsymbol{a}_x(t)=e^{\sigma_x t}\,\boldsymbol{e}_x$. Depending on the values n_x, this ansatz gives a local

eigensystem with the two eigenvalues

$$\sigma_x^{(1)} = 0\,, \tag{10a}$$

$$\sigma_x^{(2)} = f_x^a - f_x^b\,, \tag{10b}$$

and the corresponding eigenvectors

$$\boldsymbol{e}_x^{(1)} = \left[-f_x^b/f_x^a \;,\; 1\right]^T\,, \tag{11a}$$

$$\boldsymbol{e}_x^{(2)} = \left[-1 \;,\; 1\right]^T\,, \tag{11b}$$

spanning the *phase space* (a, b) of the system (c.f. main text Fig. 1b). The first eigenpair again defines a local *center space*, where the eigenvector $\boldsymbol{e}_x^{(1)}$ is tangent to the line of fixed points. The second eigenpair now defines the *local* stability of fixed points against perturbations that locally preserve the respective total mass density n_x. For each fixed n_x, the eigenvector $\boldsymbol{e}_x^{(2)}$ spans a 1-simplex defined by $a_x + b_x = n_x$. This is the *local phase space* of the compartment at position x to which its dynamics remains confined due to mass conservation (in the absence of diffusion). The eigenvalue $\sigma_x^{(2)}$, which is a function of n_x, defines the stability of these local equilibria. Taken together, this identifies the *local mass density* n_x as a *local control parameter*: For any point x in space we can reduce the local dynamics to the local phase space via $f(a, b) = f(a, n_x - a) =: f(a; n_x)$ such that the nonlinear dynamics reduces to that of a general one-dimensional dynamical system with the control parameter n_x. Hence, all co-dimension one bifurcation scenarios can be realised by variation of n_x, depending on the choice of the nonlinear function $f(a, b)$.

All of the above considerations on local equilibria are in a straightforward fashion generalised to systems with s conserved chemical species with respective conserved mass densities $n_x^{(\alpha)}(t)$, $\alpha \in S$. The corresponding local equilibria are then controlled by S independent local mass densities which grants access to co-dimension S bifurcations. For the Min dynamics (and similar intracellular protein dynamics) the notion of local equilibria needs to be further generalised as it couples dynamics on a reactive surface (membrane) with some bulk (cytosol). The subtleties arising in such cases will be discussed in Sec. VI A.

B. Dynamics with diffusive coupling

Next we analyse the effect of diffusion on the system's dynamics. Since lateral diffusion induces spatial redistribution of n_x, its role becomes that of a *dynamic control variable* which we will now investigate in the context of lateral instabilities. Returning to the full reaction-diffusion system, Eq. (1), and assuming a spatially uniform initial distribution of the total mass density, $n_x(0) = \bar{n}$, we can generalise the Jacobian to contain the diffusive part:

$$\mathcal{J}_x \to \mathcal{J}_q = \begin{bmatrix} f^a - D_a q^2 & f^b \\ -f^a & -f^b - D_b q^2 \end{bmatrix}. \tag{12}$$

The corresponding linearised system reads $\partial_t\,\delta\boldsymbol{a}_q = \mathcal{J}_q\,\delta\boldsymbol{a}_q$, and is solved by the separation ansatz $\delta\boldsymbol{a}_q \propto e^{\sigma_q t}\cos qx$. The eigenvalues are given by

$$\sigma_q^{\pm} = \frac{1}{2}\left(\tau_q \pm \sqrt{\tau_q^2 - 4\delta_q}\right)\,, \tag{13}$$

where τ_q and δ_q denote the trace and determinant of the Jacobian, respectively:

$$\tau_q := \operatorname{tr}\mathcal{J}_q = (f^a - f^b) - (D_a + D_b)\,q^2\,, \tag{14a}$$

$$\delta_q := \det\mathcal{J}_q = (D_a f^b - D_b f^a)\,q^2 + D_a D_b\,q^4\,. \tag{14b}$$

For wavenumber $q=0$, one recovers the results of the well-mixed case discussed above, Eq. (5): $(\sigma_q^+,\sigma_q^-)|_{q=0} = (\sigma^{(1)},\sigma^{(2)})$ for $\sigma^{(2)}<0$, and $(\sigma_q^+,\sigma_q^-)|_{q=0} = (\sigma^{(2)},\sigma^{(1)})$ for $\sigma^{(2)}>0$ (note that σ_q^+ is always the larger of the two eigenvalues). Now we are interested in the stability of a spatially uniform state against spatially non-uniform perturbations, i.e. the dynamics of modes with $q>0$. There are special wave vectors where the stability is marginal, $\sigma_q^{\pm}=0$, or equivalently $\det\mathcal{J}_q=0$. They are given by

$$q_{\min} = 0,\ q_{\max} = \sqrt{\frac{D_b f^a - D_a f^b}{D_a D_b}}\,, \tag{15}$$

provided that $D_b f^a - D_a f^b > 0$; otherwise the spectrum is marginal only at $q_{\min}=0$. From Eq. (13) one reads off that the condition on the determinant of the Jacobian, $\det\mathcal{J}_q \le 0$, defines a band $[0, q_{\max}]$ of unstable modes, where $\operatorname{Im}[\sigma_q^{\pm}]=0$ and $\sigma_q^+\ge 0$; see Supplementary Fig. 1 A for examples of dispersion relations. By solving $\frac{d}{dq}\det\mathcal{J}_q=0$ at $q_{\min}$ and $q_{\max}$ we find that the lateral instability always occurs first at the critical wavenumber $q_c=0$, c.f. [1].

We have to distinguish between the cases $\sigma^{(2)}<0$ and $\sigma^{(2)}>0$, where the uniform state is stable and unstable with respect to spatially uniform perturbations (conserving mass), respectively. The dispersion relations for these two cases are illustraded in Supp. Fig. 1 A. For $\sigma^{(2)}<0$, where all (spatially uniform) local equilibria are stable, the lateral instability is of type-II in the classification scheme of Cross and Hohenberg [2] with the growth rate at $q=0$ always zero: $\sigma^+_{q=0}=\sigma^{(1)}=0$, see Supp. Fig. 1 A (left). In contrast, for $\sigma^{(2)}>0$, where all (spatially uniform) local equilibria are unstable, the lateral instability is of type-III with the growth rate at $q=0$ positive: $\sigma^+_{q=0}=\sigma^{(2)}\ge 0$, see Supp. Fig. 1 A (right). As discussed next, both linear instabilities, despite of belonging to different classes, induce dynamics facilitated by the spatial redistribution of total mass density.

Let us first consider the case where the local equilibria are spatially uniform and stable. In this case the local eigenvalue (encoding *local stability* in *local phase space*) is negative: $\sigma^{(2)}<0$. Then, the eigenvalue $\sigma^{(1)}=0$, with the corresponding eigenvector $\boldsymbol{e}^{(1)}$ tangent to the line of fixed points (nullcline), determines the stability of the uniform state ($\sigma^+_{q=0}=\sigma^{(1)}=0$) with respect to uniform perturbations that alter the total mass in the system such that the system is shifted along the line of fixed points. Once shifted by a perturbation that breaks mass conservation the system remains in the local phase space, within which the stability is given by the eigenvalue $\sigma^{(2)}<0$. This case corresponds to the classical lateral

instability as considered by Turing: The system is stable without diffusive coupling, and lateral diffusive coupling leads to the formation of a finite band $[0, q_{\max}]$ of unstable modes for $f_a/D_a > f_b/D_b$. Since the instability occurs first at $q_c = 0$, we can assume q to be small at onset, and expand the eigenvector in orders of q^2. We find

$$\boldsymbol{e}^{(1)} = \boldsymbol{e}^{+}_{q=0} \rightarrow \boldsymbol{e}^{+}_{q} = \boldsymbol{e}^{(1)} - \frac{f^b}{f^a}\,\frac{D_b - D_a}{|\sigma^{(2)}|}\,q^2 \begin{pmatrix} 1 \\ 0 \end{pmatrix} + \mathcal{O}(q^4), \tag{16}$$

where $\boldsymbol{e}^{(1)}$ is tangent to the line of fixed points (center space).

What does the direction of this eigenvector reveal about the spatial redistribution of mass? The growth of any unstable mode q implies an increase of the densities $a(x,t)$ and $b(x,t)$ at the maxima and a reduction at the minima. If the growth of one density (say $a(x,t)$) at some point in space x is not balanced by the same decrease of the other density ($b(x,t)$) mass is being redistributed in space, and the local total density $n_x(t)$ becomes a dynamical *control variable*. The distance of redistribution is then given by the distances between minima and maxima of the unstable mode q, i.e. by half a wavelength π/q. The entries of the eigenvector of a mode q are the coefficients (pre-factors) of the modes for both species. Only if the sum of coefficients is zero no mass is being redistributed, in this case the eigenvector reads $\boldsymbol{e} = \begin{bmatrix} -1 & , & 1 \end{bmatrix}^T = \boldsymbol{e}^{(2)}$ and spans the 1-simplex $a + b = \bar{n}$. We can summarise the meaning of the eigenvector as follows (see also Supp. Fig. 1 B for an illustration of the eigenvectors): **The eigenvector parametrises, in the vicinity of the uniform steady state, the flow of density $(\mathbf{a}, \mathbf{b})$ in phase space induced by diffusive coupling between two reactors separated by half a wavelength $\pi/\mathbf{q}$ in space.**

For $\boldsymbol{e}^{+}_{q}$, two things are important to note: First, for $q > 0$, the eigenvector points away from the line of stable fixed points spanned by $\boldsymbol{e}^{(1)}$. Hence, as expected for a Turing instability, each reactor is driven away from the stable local reactive fixed point. However, as the eigenvector also points away from the local phase space (1-simplex) in which total mass density $\bar{n}$ is conserved, the total mass density becomes time- and concomitantly also space-dependent, i.e. $\bar{n} \rightarrow n_x(t)$. Therefore, as each reactor is driven away form its local equilibrium, the equilibrium (its position and potentially its stability) also changes dynamically. As a consequence, the flow field representing the dynamical system (reactor) becomes nonuniform in time and space, and the local control parameter n_x becomes a dynamic control variable $n_x(t)$ with dynamics driven by the lateral instability. As we will see in the following, this result is not specific to the scenario of a Turing type instability but rather generic for mass-conserved reaction-diffusion systems.

The second type of instabilities that can occur in the two-component reaction-diffusion system considerer here is defined by locally unstable equilibria, see Supp. Fig. 1 A (right). In this case the destabilisation occurs locally such that $\sigma^{+}_{q=0} = \sigma^{(2)} > 0$. By expanding the eigenvectors in orders q^2 we find a remarkably similar result as in Eq. 16:

$$\boldsymbol{e}^{(2)} = \boldsymbol{e}^{+}_{q=0} \rightarrow \boldsymbol{e}^{+}_{q} = \boldsymbol{e}^{(2)} + \frac{D_b - D_a}{|\sigma^{(2)}|}\,q^2 \begin{pmatrix} 1 \\ 0 \end{pmatrix} + \mathcal{O}(q^4). \tag{17}$$

For $D_a \neq D_b$, the spatial coupling induces a change in the total mass density $n_x(t)$ as well. Hence, even if the destabilisation of the uniform state occurs locally, we find that a lateral instability ($q > 0$) still induces dynamics in the local equilibria, just as in the previously discussed case of the Turing instability.

For the particular case where the diffusion constants are equal, we note that the total density obeys the simple diffusion equation, $\partial_t n_x(t) = D\partial_x^2 n_x(t)$, and hence will relax to a spatially uniform distribution for no-flux boundary conditions. However, in the presence of an external mass flux, the total density will tend towards some spatial gradient whose magnitude depends on the strength of this external flux. In this paper we will restrict ourselves to closed systems without external fluxes. We suppose that generalisations to include the additional effects of external fluxes are highly interesting and deserve further study.

C. Type-II instabilities in mass–conserved reaction diffusion systems

The type-II instability in the classification scheme by Cross and Hohenberg [2] is associated with the presence of conservation laws. It is important to realize that a lateral instability of type-II only implies that the system will most likely satisfy a conservation law of some sort. However, in the literature on pattern formation one often finds statements of the reverse, namely that the presence of a conservation law *necessitates* any lateral instability of the system to be of type-II. In particular, it is often assumed that in any system with a conservation law the eigenvalues of the zero mode $q = 0$ need to be zero, i.e. the system needs to be neutrally/marginally stable with respect to spatially uniform perturbations. As we have shown mathematically in the previous section there is indeed a zero eigenvalue for the mode $q = 0$. Its eigenvector is tangent to the line of fixed points ($f = 0$). However, we have also shown that the other eigenvalue of the zero mode ($q = 0$) is not generally zero but encodes the *local stability* of the system. Its corresponding eigenvector spans the local phase space where mass is conserved. Hence, spatially uniform perturbations in this direction do not break mass–conservation. If the mass–conserved system is locally unstable the dispersion relation takes the shape shown in Supp. Fig. 1 A (right), which is a type-III instability in the Cross-Hohenberg classification scheme.

For mass–conserved reaction–diffusion systems with two components the shape of the dispersion relation is limited to type-II and type-III instabilities. However, mass–conserved systems with more than two components (such as the Min system and most other intracellular pattern–forming systems) can also show lateral instabilities of type-I, see main text Fig. 2a (note that the zero mode ($q = 0$) is still marginally stable but the band of unstable modes is bound from below at a finite wavenumber). Hence, our findings show that mass–conservation does not impose any restrictions on the Type of the dispersion relation within the Cross-Hohenberg classification.

Strikingly, we find that the phenomenology of the Min dynamics does not appear to be related to the type of the dispersion relation in any way (see main text).

II. WAVE–PINNING IN THE MASS–REDISTRIBUTION FRAMEWORK

A. The concept of wave–pinning in the literature

The term wave-pinning refers to the mathematical construction of a polarized stationary state in a certain class of models for cell polarity [3, 4]. The concept originated from the study of propagating wavefronts in the classical nonlinear dynamics literature. For general bistable systems without mass–conservation such wavefronts are interfaces between two (uniform) stable states and propagate at a constant speed. The general idea underlying wave–pinning is that a propagating wavefront is *pinned* at a fixed location in space due to global mass constraints. The concept was introduced for mass-conservative two-component systems as considered in section I. The mathematical construction is based on two assumptions: First, the faster diffusing component (cytosolic) is considered in the limit of infinitely fast diffusion. The density profile of this component is therefore assumed to be spatially uniform. Second, the ensuing system is assumed to be bistable when the faster diffusing component is considered as a parameter. The wavefront solution of this system is constructed with the well-known rolling–ball–analogy (e.g. see [1]), where both stable states mark the start- and end-point of a fictitious ball's trajectory.

A main claim in the literature is that a wave–pinning pattern is distinct from any mechanism related to Turing instabilities or Turing patterns. In the following we will study the original wave-pinning model [3] within our mass–redistribution framework, discuss the origin of the aforementioned statement, and argue that it is based on a conceptual misinterpretation of local stability in the limit of infinite cytosolic diffusion.

B. Wave–pinning is based on mass–redistribution

The wave–pinning phenomenon has been introduced for a Rho GTPase model by Mori et al. [3]. The model considers two diffusive components in a one–dimensional domain (representing the cell) of length L:

$$\partial_t a(x,t) = D_a \partial_x^2 a + f(a,b), \tag{18}$$

$$\partial_t b(x,t) = D_b \partial_x^2 b - f(a,b). \tag{19}$$

The authors consider a reaction term with positive feedback described by a Hill term

$$f(a,b) = b\left(k_0 + \frac{\gamma a^2}{K^2 + a^2}\right) - \delta a. \tag{20}$$

The parameters with their corresponding biological meaning and values are given in Table I. Due to mass conservation we additionally need to specify the total mass in the system:

$$\int_0^L (a+b)\,\mathrm{d}x = \int_0^L n_x\,\mathrm{d}x = N. \tag{21}$$

D_a	0.1 $\mu m^2 s^{-1}$	membrane diffusion
D_b	10 $\mu m^2 s^{-1}$	cytosolic diffusion
L	10 μm	cell length
δ	1 s^{-1}	inactivation rate (GAP hydrolysis)
γ	1 s^{-1}	GEF activation rate
k_0	0.0.67 s^{-1}	baseline GEF activity
K	1 μm^{-1}	saturation parameter

TABLE I: Parameters of the wave–pinning model [3].

Note that we are using our naming conventions here, in the original model [3] total mass is denoted by C.

With the model definition in place, we can now proceed with the analysis of the underlying mechanism. To this end we first look at the $f = 0$ nullcline in the phase space (a, b). For the given reaction term (Eq. 20), the nullcline has a characteristic N-shape (Supp. Fig. 1B). In the limit of infinite cytosolic diffusion ($D_b \to \infty$) the spatial distribution of the b component is uniform, i.e. $b(x, t) = b(t)$. In the phase space (a, b) the whole system will, therefore, be constrained to lines with constant b. We will refer to these lines as the subspace of the polarized state.

The construction of the wave–pinning pattern is based on the concept of bistabilty. For the N-shape of the $f = 0$ nullcline there is a range of b values for which the system admits three intersections between the subspace of the polarized state and the nullcline. Let us denote these intersections by $a^*_-(b^*) < a^*_m(b^*) < a^*_+(b^*)$. In the wave–pinning literature, bistabilty refers to the existence of these three intersections. It is important to realize that these states are local equilibria for *different* values of the local total density n_x. One part of the system is in the high density state $a^*_+(b^*)$ where the local total density is $n_+ = a^*_+ + b^*$. The other part of the system is in a low density state $a^*_-(b^*)$ with $n_- = a^*_- + b^*$. Since b^* is constant and $a^*_-(b^*) < a^*_+(b^*)$, it follows that this construction is based on a spatially non-uniform distribution of total mass density n_x: the wave–pinning pattern is a pattern of local equilibria by construction, see Supp. Fig. 2 C (bottom). Moreover, since there is only one fixed point for each spatially uniform $n_x = \overline{n}$, there is no bistabilty in the local phase space $a + b = \overline{n}$. Hence, redistribution of total mass density is explicitly required to reach the wave–pinning pattern. In the wave–pinning literature one assumes that an external perturbation facilitates this mass redistribution. The perturbation induces formation of a propagating wave front that stops (becomes "pinned") due to global mass conservation. However, in stark contrast to known wave propagation phenomena in bistable media, the states (a^*_-, b^*) and (a^*_+, b^*) do no exist a priori, but are created by externally induced mass redistribution. Considering that mass redistribution is the main feature of a lateral (Turing) instability, it is surprising that wave–pinning is supposed to be unrelated to any mechanism

based on Turing instability.

To shed light on this matter let us analyse the model and its local and lateral stability in full detail. First, let us remind the reader that a Turing instability is defined by the local stability of the system and induced by lateral diffusive coupling alone. Because the Turing instability is an instability of a spatially uniform state, we will denote spatially uniform states by (a^*, b^*) instead of $a^*(b^*)$. The latter notation that is used by the authors of the wave–pinning model (cf. [3]) implies that b^* is the control parameter, while the actual control parameter is $\overline{n}$. From the previous discussion in section I we know that any lateral instability (regardless of the local stability) is based on redistribution of total density which leads to a movement of local equilibria. The main requirement for redistribution of total density are unequal diffusion coefficients. This is clearly fulfilled for the wave–pinning model, in particular, in the case of infinitely fast cytosolic diffusion.

Next, we need to check the local stability of the uniform steady state for all values of the control parameter $\overline{n}$. For any two–component system a local equilibrium (a^*, b^*) is unstable iff

$$\sigma^{(2)} = f^a - f^b \geq 0, \tag{22}$$

where $f^a = \partial_a f|_{(a^*,b^*)}$ and $f^b = \partial_b f|_{(a^*,b^*)}$. In this case all parameters except the total mass N (which is related to the total density $\overline{n}$ through $\overline{n} = N/L$) determining the position of the local equilibria are given. A computation of $\sigma^{(2)}$ as a function of $\overline{n}$ shows that the local equilibrium $(a^*(\overline{n}), b^*(\overline{n}))$ (which is unique for any fixed choice of $\overline{n}$) is always locally stable, including the "middle" steady state (a^*_m, b^*) in the subspace of the polarized state (constant b). Therefore, a Turing instability cannot be ruled out *a priori* for the uniform steady state (a^*_m, b^*). For a locally stable two–components system a band of unstable modes (type-II instability) exists iff (see Eq. 15)

$$D_b f^a - D_a f^b > 0. \tag{23}$$

To check this condition let us first note that $-f^a/f^b$ denotes the slope of the f nullcline in the phase space (a, b), i.e.

$$\partial_a b^*(a)|_{a=a^*} = -f^a/f^b. \tag{24}$$

In addition, from Eq. 20 we obtain $f^b = k_0 + \frac{\gamma a^2}{K^2+a^2} > 0$ for all parameter choices. Then we can immediately read off from the N-shape of the nullcline that $f^a > 0$ in general for all middle steady states (a^*_m, b^*), see Supp. Fig. 2 A. In addition, note that f^a and f^b are independent of the diffusion coefficients D_b and D_a. For the assumption of infinite b diffusion $(D_b \to \infty)$, on which the construction of the wave–pinning solution is based, it immediately follows from Eq. 23 that (a^*_m, b^*) is always laterally (Turing) unstable, and from Eq. 15 that there is a band of unstable modes that extends to $q_{\max} = \sqrt{f^a/D_a}$. Hence, the assumptions on which wave–pinning is based (bistability for constant b) guarantees a Turing instability for this type of models (characterized by the N-shape of the f nullcline), cf. Supp. Fig. 2 A.

Up to this point we have clearly established that the wave–pinning model does admit a Turing instability. Moreover, wave–pinning relies on mass–redistribution in order to create

bistability of local equilibria in the subspace of the polarized state (constant b, see Supp. Fig. 2 A). Our findings also show that any lateral instability generically leads to the redistribution of local total density and thereby the movement of local equilibria. Taken together, this implies that the possibility of wave–pinning and the presence of a Turing instability is not a mere coincidence, but that both phenomena are based on the same self–organization mechanism. Our previous analysis of the general two–component model (Eq. 1) revealed that any unstable mode $\cos(qx)$ causes the redistribution of local total density, and that the ensuing mass transport is associated with a *direction* in phase space (a, b) given by the eigenvector $\boldsymbol{e}_q^+$ (Eq. 16) of the mode, i.e. $\begin{bmatrix} a(x,t) & , & b(x,t) \end{bmatrix}^T \sim \boldsymbol{e}_q^+ \exp(\sigma_q^+ t) \cos(qx)$ at onset of the lateral instability. In this previous section we have mainly used this result to show that any unstable mode causes the redistribution of local total density n_x, as $\boldsymbol{e}_q^+$ points away from the subspace where mass is conserved $a^* + b^* = \overline{n}$ (local phase space). The particular direction of $\boldsymbol{e}_q^+$ had no specific relevance in this general discussion. However, we know that (for $D_b \to \infty$) the subspace containing the final pattern is a line for constant b in the phase space. Hence, the subspace for the polarized state is spanned by the vector $\begin{bmatrix} 1 & , & 0 \end{bmatrix}^T$. Let us assume that the system is initially in the uniform (Turing unstable) steady state (a_m^*, b^*). To reach the polarized state the local total density needs to be redistributed such that the dynamics approach the states (a_-^*, b^*) and (a_+^*, b^*). Since we assume infinite diffusion of component b ($D_b \to \infty$) it only matters how the eigenvectors $\boldsymbol{e}_q^+$ depend on D_b. From Eq. 16 we directly read off $\boldsymbol{e}_q^+ \sim \begin{bmatrix} D_b q^2 & , & 1 \end{bmatrix}^T$. Hence, in the limit $D_b \to \infty$ the normalized eigenvector $\boldsymbol{e}_q^+$ spans the subspace of the polarized state, i.e.

$$\lim_{D_b \to \infty} \boldsymbol{e}_q^+ = \begin{bmatrix} 1 & , & 0 \end{bmatrix}^T, \ \forall q. \tag{25}$$

We conclude that the polarized state originates from a lateral (Turing) instability, and note that this analytical result is supported by simulations, see Supp. Fig. 2 C.

Of course, this does not imply that a Turing unstable uniform steady state is strictly required for the polarized state to exist. It has already been pointed out by Goryachev and Leda [5] (also see [6]) that a Turing stable uniform state near a subcritical Turing instability should admit a polarized state, since subcritical bifurcations are a sign for excitability. Indeed the authors of the original wave–pinning model consider a Turing stable uniform solution (a_-^*, b^*) as the initial base state, and observe that the polarized state is reached if this state is sufficiently perturbed. Heuristically speaking, this is possible if a perturbation of the local total density n_x puts a sufficiently large part of the system in the basin of attraction of the state (a_+^*, b^*) by increasing $n_x(0)$ locally beyond $n_m = a_m^* + b^*$, i.e. $n_x(0) > n_m$ for some range of x values at time $t = 0$. It is important to realize that such a choice of initial conditions where the system is spatially distributed between the basins of attraction of (a_-^*, b^*) ($n_x(0) < n_m$) and (a_+^*, b^*) ($n_x(0) > n_m$) is exactly the action of the lateral (Turing) instability at the uniform steady state (a_m^*, b^*). The only difference is that in the excitable case, an external stimulus guides the system into the basin of attraction of the polarized state, whereas in the second case, this guidance is self–organized by the Turing instability.

However, even if the system is in an excitable state, a variation of system parameters (e.g. a change of total density $\bar{n}$) will *always* (due to the shape of the nullcline) be able to render the excitable state laterally unstable such that pattern formation becomes self-organized.

Now that we have established the mechanistic connection between the Turing instability and the wave–pinning phenomenon, two main question remain. The first questions concerns the length scale of the fastest growing mode which sets the length scale at onset. The second question concerns the misunderstanding on which basis the uniform solution (a_m^*, b^*) has been identified as unstable and therefore ruled out as a candidate for a Turing instability. Because the answers to both questions turn out to be connected we will discuss them together in the following section. Again, the realization that the key physical process for pattern formation is mass redistribution will turn out to be crucial.

C. Local and lateral stability in the limit of infinitely fast diffusion

The fastest growing mode q_c from the band of unstable modes ($q_{\min} < q_c < q_{\max}$) always sets the initial length scale of the pattern forming process in the linear regime. For lateral instabilities in mass–conserving two–component models with a locally stable uniform state (Turing) the band of unstable modes always extends down to the zero mode, i.e. $q_{\min} = 0$ (cf. Eq. 15). It has been previously been realized by Trong et al. [6] that the position of the fastest growing mode q_c strongly depends on the value of the fast diffusion coefficient (D_b in our case). Indeed, one can analytically derive from the q-dependent spectrum of the Jacobian (Eq. 12) that q_c approaches the zero mode as D_b approaches infinity, i.e.

$$\lim_{D_b \to \infty} q_c = 0, \tag{26}$$

while maintaining a positive growth rate, i.e.

$$\lim_{D_b \to \infty} \sigma^+_{q_c} = f^a > 0. \tag{27}$$

Hence, in the limit $D_b \to \infty$ the mode with longest wavelength (which is infinite in an infinite system) becomes the fastest growing mode. The growth rate $\sigma^+_{q\to 0} > 0$ converges towards f^a, and not towards zero. The system remains neutral stability for any finite $D_b < \infty$. Only for $D_b = \infty$ does the dispersion obtain the characteristic shape with a maximum at $q = 0$, i.e.

$$\lim_{D_b \to \infty} \sigma^+_q = f^a - D_a q^2, \tag{28}$$

which represents a prototypical type-III instability within the Cross-Hohenberg classification scheme, see Supp. Fig. 2 B. It is absolutely crucial to realize that this *discontinuously displaced zeroth Fourier mode* [6] does not represent nor alter the local stability of the system which is still determined by $\sigma^{(2)} = f^a - f^b$, and is independent of any lateral diffusion process (e.g. D_b) by definition of locality (fixed x). However, the pathological shape of the dispersion relation (Supp. Fig. 2 B) in the limit $D_b \to \infty$ with an unstable zero mode appears to be the reason why the middle fixed point (a_m^*, b^*) has been ruled out as a candidate for a Turing

instability. This also emphasizes that local stability and therefore the condition for a Turing instability cannot be inferred from the dispersion relation (at $q = 0$) in such limiting cases, but has to be considered explicitly by calculating the local stability in the local phase space of the uniform state (Eq. 22).

Furthermore, we note that the shape of the dispersion relation in the limit $D_b \to \infty$ does reveal additional insight about the mechanism underlying wave–pinning, when considered in the context of mass redistribution. As discussed in the previous sections, any laterally unstable mode induces a redistribution of local total density on the length scale π/q (the distance between minima and maxima of a mode $\sim \cos qx$). Let us consider a system with length L ($-L/2 < x < L/2$) and no–flux boundary conditions at $x = \pm L/2$. Then the spectrum of modes with finite wave length will be limited to the discrete set $\{\sin(n\pi/Lx) \mid n = 1, 2, ...\}$. Note that the polarized pattern is represented by the mode with the longest wave length ($n = 1$) with a minimum at $x = -L/2$ and a maximum at $x = +L/2$ (or vice versa). As the wave length of the fastest growing mode increases with D_b we can guarantee for any system length L that the the first mode ($n = 1$) will be the fastest growing mode for sufficiently high D_b, i.e. that local total density is redistributed the fastest from $x = -L/2$ to $x = +L/2$ (or vice versa). This is *exactly* the requirement needed for the uniform system to approach the polarized wave–pinning state.

This discussion also reveals the physically correct interpretation of the dispersion relation at $q = 0$ in the (pathological) limit $D_b \to \infty$ (Supp. Fig. 2). In this limit the fastest growing mode transports local total density from $x = -L/2$ to $x = +L/2$ (or vice versa) for any system length L. Only in this limit the latter remains to be the case for $L \to \infty$, where the fastest growing mode $q_c = \pi/L$ induces mass-redistribution from $x = -\infty$ to $x = +\infty$. Clearly this cannot represent any meaningful physical process. Hence, it becomes evident that the dispersion relation at $q = 0$ defines a lateral instability (from $x = -\infty$ to $x = +\infty$) and does not represent the local stability of the uniform state (which is independent of diffusion by definition, and still encoded by 22). This example shows that the distinction between these two physically distinct properties of a system (local and lateral stability) needs to be carefully considered. In this case the distinction was obfuscated by the limit $D_b \to \infty$, where system becomes laterally coupled on an instantaneous time scale ($\sqrt{D_b/L^2}$), i.e. lateral mass transport can be instantaneous across any distance and the dynamics is effectively "delocalized".

III. MIN PROTEIN DYNAMICS AND THE EFFECT OF SYSTEM GEOMETRY

A. Reaction-diffusion equations for the skeleton model of Min dynamics

We use a mathematical model [7, 8] for the Min system that accounts for the molecular interactions that are believed to be essential for the Min protein dynamics. This model includes the following set of chemical reactions:

1. The attachment of cytosolic MinD-ATP, u_{DT}, to the membrane with rate constant k_D.
2. The recruitment of cytosolic MinD-ATP, u_{DT}, to the membrane by membrane bound MinD, u_d, with rate constant k_{dD}.
3. The formation of membrane bound MinDE complexes, u_{de}, through the recruitment of cytosolic MinE, u_E, by membrane bound MinD, u_d, with rate constant k_{dE}.
4. The detachment and decay of membrane bound MinDE complexes, u_{de}, into cytosolic MinD-ADP, u_{DD}, and MinE, u_E, with rate k_{de}.
5. The reactivation of cytosolic MinD-ADP, u_{DD}, by nucleotide exchange to MinD-ATP, u_{DT}, with rate λ.

All components are able to diffuse in their respective domains (cytosol or membrane). Since only the distinction between cytosolic and membrane diffusion is important for the dynamics, and since the diffusion coefficients with a domain (cytosol or membrane) are very similar for different proteins, we only distinguish between cytosolic and membrane diffusion with diffusion constants D_c for the cytosol and D_m for the membrane, respectively.

In previous work [8], the mathematical model has been generalised to complex system geometries with bulk-boundary coupling (this will be discussed in this section below), and subsequently applied to account for

- the transition from pole-to-pole oscillations to (multi-node) stipe oscillation in filamentous cells [8],
- oscillations with rotating oscillation axis in nearly spherical cells [8],
- the temperature dependence of the oscillation period [8],
- robustness of the intracellular pattern agains inhomogeneities in the lipid composition (affecting the attachment process) [8],
- optimisation of the time-average membrane density profile for mid-cell localisation [8],
- traverse oscillations in broad rectangular cells [9, 10],
- multi-stability of various longitudinal and transversal patterns in large rectangular cells [9, 10].

This success to consistently reproduce and explain a broad range of experimentally observed features of the Min system suggests that the underlying molecular interaction are indeed essential for the Min protein dynamics. As new experimental data on the molecular interactions of Min proteins becomes available, the kinetic processes assumed in the model can be further refined (e.g. by replacing one-step processes with multi-step processes). In the latter case we would expect that the original network would be contained in a detailed model as a limiting case. For this reason we refer to the reaction network outlined above as the *skeleton network*, and *skeleton model* respectively.

In coordinate free form (with index c or m denoting that an operator acts in the cytosol or at the membrane, respectively) the ensuing system of partial differential equations for the skeleton model reads:

$$\partial_t u_{DD} = D_c \nabla_c^2 u_{DD} - \lambda u_{DD}\,, \tag{29a}$$

$$\partial_t u_{DT} = D_c \nabla_c^2 u_{DT} + \lambda u_{DD}\,, \tag{29b}$$

$$\partial_t u_E = D_c \nabla_c^2 u_E\,, \tag{29c}$$

$$\partial_t u_d = D_m \nabla_m^2 u_d + f_d(u_d, \tilde{u}_{DT}, \tilde{u}_E), \tag{29d}$$

$$\partial_t u_{de} = D_m \nabla_m^2 u_{de} + f_{de}(u_{de}, u_d, \tilde{u}_E)\,, \tag{29e}$$

where the chemical reactions on the membrane are given by the nonlinear functions

$$f_d(u_d, \tilde{u}_{DT}, \tilde{u}_E) := (k_D + k_{dD} u_d)\, \tilde{u}_{DT} - k_{dE}\, u_D\, \tilde{u}_E\,, \tag{30a}$$

$$f_{de}(u_{de}, u_d, \tilde{u}_E) := k_{dE}\, u_D\, \tilde{u}_E - k_{de}\, u_{de}\,, \tag{30b}$$

with $\tilde{u}_i$ denoting the respective cytosolic densities right at the membrane. These equations are complemented by nonlinear reactive boundary conditions at the membrane surface stating that the chemical reactions involving both membrane-bound and cytosolic proteins equal the diffusive flux onto ($-$) and off ($+$) the membrane (the index n denoting the outward normal vector at the boundary)

$$D_c \nabla_n u_{DD}|_m = k_{de}\, u_{de} =: f_{DD}\,, \tag{31a}$$

$$D_c \nabla_n u_{DT}|_m = -(k_D + k_{dD} u_d)\, \tilde{u}_{DT} =: f_{DT}\,, \tag{31b}$$

$$D_c \nabla_n u_E|_m = k_{de}\, u_{de} - k_{dE}\, u_D\, \tilde{u}_E =: f_E\,, \tag{31c}$$

and no-flux boundary condition at any non-reactive surfaces (denoted by the index s)

$$D_c \nabla_n u_{DD}|_s = 0\,, \tag{32a}$$

$$D_c \nabla_n u_{DT}|_s = 0\,, \tag{32b}$$

$$D_c \nabla_n u_E|_s = 0\,. \tag{32c}$$

The above set of reaction-diffusion equations locally conserve the total mass of MinD as well as MinE. This implies that the spatial averages, $\overline{[\mathrm{MinD}]}$ and $\overline{[\mathrm{MinE}]}$, of the total densities of MinD and MinE obey the relation

$$\overline{[\mathrm{MinD}]}\,\Omega = \int_\Omega \mathrm{d}c\ (u_{DD} + u_{DT}) + \int_{\delta\Omega} \mathrm{d}m\ (u_d + u_{de})\ , \tag{33a}$$

$$\overline{[\mathrm{MinE}]}\,\Omega = \int_\Omega \mathrm{d}c\ u_E + \int_{\delta\Omega} \mathrm{d}m\ u_{de}\,, \tag{33b}$$

where $\int_\Omega \mathrm{d}c$ and $\int_{\delta\Omega} \mathrm{d}m$ signify integration over the whole cytosolic volume Ω and membrane surface $\delta\Omega$, respectively. The values of the overall masses of these conserved quantities needs to be specified (in the simulation through the initial condition).

The advantage of such a general (coordinate-free) model definition is that it can be adjusted to any system geometry, allowing to consistently use the same model for different experimental setups. For the *in-vitro* experiments a simple box geometry is typically used, where the reactive lipid bilayer (membrane) is located at the bottom of the box, and all other boundaries are reflective. Since the lateral extension of *in-vitro* box geometries is typically very large $\mathcal{O}(10^3 \mu m)$ compared to the wave length of the pattern $\mathcal{O}(10\,\mu m)$, we will perform simulations in an intermediate sized computational box $\mathcal{O}(10^2 \mu m)$ and employ periodic boundary conditions. The height h of the experimental box geometry is similarly very large $\mathcal{O}(10^3 \mu m)$ such that the dynamics perpendicular to the membrane cannot be neglected for two main reasons that we will discuss in the following subsection.

The parameter values used in the simulations are given in Table II.

TABLE II: **System parameters**. The values of the diffusion coefficients and protein densities are chosen in accordance with experimental data [11]. The kinetic rate constants are chosen within the order of magnitude of the values fitted to the *in vivo* dynamics [8, 10] to reproduce the *in-vitro* phenomenology qualitatively and the wavelengths and -velocities quantitatively within the order of magnitude of the experimental data.

Parameter	Symbol	Value
MinD and MinE cytosol diffusion	D_c	$60\,\mu m^2 s^{-1}$
MinD and MinDE membrane diffusion	D_m	$0.013\,\mu m^2 s^{-1}$
MinD mean total density	$\overline{[\mathrm{MinD}]}$	$638\,\mu m^{-3}$
MinE mean total density	$\overline{[\mathrm{MinE}]}$	$410\,\mu m^{-3}$
MinD attachment rate constant	k_D	$0.065\,\mu m s^{-1}$
MinD recruitment rate constant	k_{dD}	$0.098\,\mu m^3 s^{-1}$
MinE recruitment rate constant	k_{dE}	$0.126\,\mu m^3 s^{-1}$
MinDE detachment rate	k_{de}	$0.34\,s^{-1}$
Nucleotide exchange rate	λ	$6\,s^{-1}$

B. Relevance of the cytosolic bulk for the spatiotemporal membrane dynamics

The dynamics of most intracellular processes, and in particular the Min dynamics, involves a coupling between dynamics on a membrane surface and a cytosolic volume. Biochemical interactions, with the exception of nucleotide exchange, are confined to the vicinity of the membrane. At first sight, one might therefore suppose that it is straightforward to eliminate the cytosolic bulk from the dynamics and consider it simply as a passive particle reservoir. Though there are certain limits where this is indeed possible, in general, however, the bulk dynamics plays a key role for the spatiotemporal dynamics and can not be disregarded. In the following we will illustrate the underlying physics for two simple analytically tractable cases, and discuss general implications for reaction–diffusion systems with bulk–boundary coupling.

1. The attachment rate constrains the reduction of the bulk dimension

Consider a diffusion process normal to the membrane in a one-dimensional column of height h. Then for a single protein species with line density $c(z,t)$ and diffusion constant D_c, the dynamics are given by a one-dimensional diffusion equation

$$\partial_t c(z,t) = D_c \nabla_z^2 c(z,t)\,. \tag{34}$$

At one end of the column (the reactive membrane) we consider an attachment process where cytosolic particles attach to the membrane with a rate k_{on}. Then local mass conservation implies a (Robin) boundary condition which accounts for the balance of reactive flux on the membrane with diffusive in the cytosol flux due to ensuing density gradients,

$$-k_{\mathrm{on}}\, c(0,t) + D_c \nabla_z c(z,t)|_{z=0} = 0\,. \tag{35}$$

This 'reactive' boundary condition is complemented by reaction kinetics on the membrane

$$\partial_t m(t) = k_{\mathrm{on}}\, \tilde{c}(t)\,, \tag{36}$$

where $m(t)$ denotes the membrane density and we have introduced $\tilde{c}(t) = c(0,t)$ for the cytosolic density right at the membrane. Note that the Robin boundary condition, Eq.(35), clearly shows that inevitably any reactive coupling between the cytosol and the membrane (here attachment to the membrane) leads to gradients in the cytosolic bulk. The corresponding length scale can be read off (by simple dimensional analysis) from Eq.(35) as

$$\ell_{\mathrm{on}} := D_c/k_{\mathrm{on}}\,. \tag{37}$$

At the other end (the surface of the cytosolic solution), the system is assumed to be closed which implies a reflective boundary condition

$$D_c \nabla_z c|_{z=h} = 0\,. \tag{38}$$

We now ask under what conditions one may disregard the diffusive dynamics normal to the membrane. To this end, we define the spatial average of the cytosolic protein density as

$$\bar{c}(t) = \frac{1}{h}\int_0^h dz\, c(z,t)\,. \tag{39}$$

Combining Eq.(34) with the boundary conditions, Eq.(35) and (38), one obtains

$$\partial_t \bar{c}(t) = -\frac{k_{\rm on}}{h}\, c(0,t)\,. \tag{40}$$

This reduces to an equation for the concentration at the membrane $c(0,t) = \tilde{c}(t)$ only if one can approximate the average density by the density at the membrane, $\bar{c}(t) \approx \tilde{c}(t)$. Then one gets

$$\partial_t \tilde{c}(t) = -\frac{k_{\rm on}}{h}\, \tilde{c}(t)\,, \tag{41}$$

which is solved by $\tilde{c}(t) = \tilde{c}(0)\, e^{-t/\tau_{\rm on}}$ where the relaxation time is given by

$$\tau_{\rm on} := \frac{h}{k_{\rm on}}\,. \tag{42}$$

However, one can approximate the average density by the density at the membrane only if there are no significant gradients in the bulk. Heuristically, this requires that the penetration depth $\ell_{\rm on}$ is much *larger* that the height h of the column, $h \ll \ell_{\rm on}$. As the above reaction-diffusion equation is exactly solvable this can also been seen explicitly. With the separation ansatz $c(z,t) = \varphi(t)\zeta(z)$, and the separation parameter σ one gets

$$\partial_t \varphi(t) = -\sigma\, \varphi(t)\,, \tag{43a}$$

$$D_c \nabla_z^2 \zeta(z) = -\sigma\, \zeta(z)\,. \tag{43b}$$

These linear equations are solved by $\varphi(t) = \varphi(0)\, e^{-\sigma t}$ and $\zeta(z) = \zeta(h)\, \cos(q(h-z))$, and linear combinations of these solutions $c(z,t)$; note that we have chosen the spatial part $\zeta(z)$ such that it already respects the reflective boundary condition at $z = h$, Eq.(38). The relaxation rate σ is related to the wave vector q by the dispersion relation (Eq.(43b))

$$\sigma = D_c\, q^2\,, \tag{44}$$

and the set of possible wave vectors $\{q_i\}$ is determined by the eigenvalue condition

$$h q_i \tan(h q_i) = \frac{h}{\ell_{\rm on}}\,, \tag{45}$$

which is obtained from the Robin boundary condition, Eq.(35). This transcendental equation may be solved graphically (or numerically). Analytic solutions are obtained in asymptotic limits only. If $h \ll \ell_{\rm on}$, we may approximate $\tan(hq) \approx hq$ to find the smallest eigenvalue as $q_1 = 1/\sqrt{h\ell_{\rm on}}$. The corresponding relaxation rate is $\tau_1 = \frac{1}{\sigma_1} = \frac{h\ell_{\rm on}}{D_c} = \frac{h}{k_{\rm on}}$, which is identical to $\tau_{\rm on}$ defined above. All other relaxation times, corresponding to larger wave vectors, are smaller and hence correspond to faster decay. Therefore, after initial transients

(resulting from some prepared initial state) have decayed, the dominant wave length is $\lambda_{\max} = \frac{2\pi}{q_1} = 2\pi\sqrt{h\ell_{\rm on}} \gg 2\pi h$, i.e. gradients on the scale of the column can be neglected. The dynamics of the longest wave length mode then corresponds to the dynamics of the average cytosolic concentration, Eq.(41), $c(z,t) \propto e^{-t/\tau_1}\cos(q_1(h-z))$; note that $\cos(q_1(h-z))$ hardly shows any z-dependence as $q_1 \ll h$. In the opposite limit, $h \gg \ell_{\rm on}$, the eigenvalues are approximately given by $hq_i = (2i-1)\frac{\pi}{2}$ with $i \in \{1,2,3,\ldots\}$ such that the largest wave length is $\lambda_{\max} = 4h$ and gradients are significant. We conclude that for the dominant slow modes (largest wave length modes) the bulk dynamics may be neglected if the penetration depth $\ell_{\rm on}$ is much larger than the column height h. For fast modes and for columns with a height larger than the penetration depth, there are significant density gradients in the bulk whose dynamics show an intricate interplay with the membrane dynamics. Hence, the cytosolic dynamics is an integral part of the system's dynamics and can not effectively be described as some passive reservoir.

All of the above may also be summarised by a simple scaling argument: The diffusive dynamics normal to the reactive membrane can be neglected if the time scale of cytosolic mixing, $\tau_{\rm diff} \sim h^2/D_c$, is much smaller than the typical time a protein suspended in the bulk needs to attach to the membrane, $\tau_{\rm on} \sim h/k_{\rm on}$. This yields the condition

$$h \ll \frac{D_c}{k_{\rm on}} = \ell_{\rm on}\,, \tag{46}$$

which the ratio of the cytosolic diffusion coefficient, D_c, and the attachment rate, $k_{\rm on}$, need to satisfy in order to justify assuming a well-mixed cytosolic volume and neglect any density gradients.

For the dynamics of the Min system *in-vitro* an upper bound for the penetration depth can be estimated from the experimental data. MinD accumulation within a traveling wave takes place on a timescale $\Delta t \approx 40s$ during which the membrane density increases by the amount $\Delta m(t) \approx 1.5 \cdot 10^4 \mu m^{-2}$. With the upper bound for the cytosolic MinD density set by the mean total density $\overline{[\mathrm{MinD}]} \approx 600\,\mu m^{-3}$, one can estimate (employing Eq.(36)) a minimal attachment rate constant $k_{\rm on,\,min} \approx \frac{\Delta m/\Delta t}{\overline{[\mathrm{MinD}]}} \approx 0.625\,\mu m/s$. With the diffusion constant $D_c \approx 60\,\mu m^2 s^{-1}$ one obtains an upper bound for the penetration depth: $\ell_{\rm on}^{\max} \approx 96\,\mu m$. Since this value is much smaller than the typical bulk height $h_{\rm exp}$ used in *in-vitro* experiments $h_{\rm exp} \approx 5 \cdot 10^3 \mu m$, one must conclude that the bulk dynamics can not be neglected. In the above crude estimate we have mot accounted for the fact that attachment is actually a nonlinear process, and that there is also constant detachment of MinD induced by MinE recruitment. Therefore, any measured effective attachment rate $k_{\rm on}$ is actually the net difference between ongoing attachment and detachment of proteins. In terms of the skeleton model, the total attachment rate is explicitly given by $k_{\rm on} = k_D + k_{dD}u_d$, where the values for the rates k_D and k_{dD} are given in Table II. Extracting the MinD membrane density u_d from our simulations (that reproduce the order of magnitude of experimental time scales) we find values ranging from a minimal value $u_{d,\min} \approx 2\,\mu m^{-2}$ to a maximal value $u_{d,\max} \approx 2.7 \cdot 10^3\,\mu m^{-2}$, and an average value of $\bar{u}_d \approx 8.3 \cdot 10^2 \mu m^{-2}$. For the penetration depth this corresponds to

an upper bound $\ell_{\text{on, max}} \approx 200\,\mu m$, a lower bound $\ell_{\text{on, min}} \approx 0.2\,\mu m$, and an average value $\overline{\ell_{\text{on}}} \approx 0.7\,\mu m$. Besides giving estimates for the value of the penetration depth, this analysis also shows several additional aspects: (i) The nonlinear nature of an attachment process has to be taken into account when a reduction of the bulk dimension is being considered. (ii) The penetration depth is a dynamic quantity which varies as the concentration of proteins on the membrane varies. Upon combining experimental data with our computational analysis we conclude that the attachment rates of Min proteins clearly forbid the reduction of the bulk dimension when accounting for *in-vitro* experiments.

2. Reduction of the bulk dimension with nucleotide exchange

A second reason why the bulk dimension cannot be reduced easily is cytosolic nucleotide exchange. MinD is released from the membrane into the cytosol in its ADP form, and is transformed back into its ATP form by nucleotide exchange with a rate that can be estimated to $\lambda \approx 6\,s^{-1}$ (c.f. [8]). This corresponds to a source-degradation process with the membrane as an MinD-ADP source, and implies that the MinD-ADP density decays exponentially into the cytosol with a *penetration depth* given by

$$\ell := \sqrt{D_c/\lambda}\,. \tag{47}$$

Since typical values of the cytosolic diffusion constant D_c for proteins is *in-vitro* of the order $60\,\mu m^2\,s^{-1}$, one estimates $\ell \approx 3\,\mu m$, which is much smaller than typical system heights h used experimentally. Hence there are protein density gradients normal to the membrane due to nucleotide exchange, and we will show next that they critically influence the chemical equilibrium at the membrane.

Consider a one-dimensional column of height h where the dynamics of MinD-ATP and Mind-ADP in the bulk is given by the following reaction-diffusion equations

$$\partial_t u_D(z,t) = D_c \nabla_z^2 u_D - \lambda u_D\,, \tag{48a}$$

$$\partial_t u_T(z,t) = D_c \nabla_z^2 u_T + \lambda u_D\,, \tag{48b}$$

where $u_D(z,t)$ and $u_T(z,t)$ denote the cytosolic density of MinD-ADP and MinD-ATP, respectively. We further assume that MinD-ATP may bind to the membrane through some nonlinear attachment process specified by an arbitrary function $f_{\text{on}}(u_m, \tilde{u}_T)$ where $\tilde{u}_T = u_T|_{z=0}$ denotes the value of the cytosolic MinD-ATP concentration at the membrane, and $u_m(t)$ signifies the MinD-ATP membrane concentration. Membrane bound MinD-ATP is assumed to transform into MinD-ADP upon detaching from the membrane through a linear process specified by the rate constant k_{off}. Then, the membrane dynamics reads

$$\partial_t u_m(t) = f_{\text{on}}(u_m, \tilde{u}_T) - k_{\text{off}}\, u_m\,. \tag{49}$$

and the corresponding reactive boundary condition at the membrane ($z = 0$), respecting local

mass conservation, is given by

$$k_{\rm off}\, u_m + D_c \nabla_z u_D|_{z=0} = 0\,, \tag{50a}$$

$$-f_{\rm on}(u_m, \tilde{u}_T) + D_c \nabla_z u_T|_{z=0} = 0\,. \tag{50b}$$

The column is assumed to be closed at $z = h$, which yields the reflective boundary conditions

$$D_c \nabla_z u_D|_{z=h} = 0\,, \tag{51a}$$

$$D_c \nabla_z u_T|_{z=h} = 0\,. \tag{51b}$$

In the following we consider the steady state. Solving the stationary diffusion equation and stationary membrane kinetics subject to the reactive and reflective boundary conditions yields for the stationary density profiles in the bulk,

$$u_D^*(z) = \tilde{u}_D^*\, \frac{\cosh\left(\frac{h-z}{\ell}\right)}{\cosh\left(\frac{h}{\ell}\right)}\,, \tag{52a}$$

$$u_T^*(z) = \tilde{u}_T^* + \tilde{u}_D^* \left[1 - \frac{\cosh\left(\frac{h-z}{\ell}\right)}{\cosh\left(\frac{h}{\ell}\right)}\right]\,, \tag{52b}$$

where $\tilde{u}_D^*$ and $\tilde{u}_T^*$ denote the stationary densities of MinD-ADP and MinD-ATP, respectively, right at the membrane ($z = 0$). These bulk profiles explicitly show that ℓ plays the role of a penetration depth into the bulk. The MinD-ADP concentration has its largest value at the membrane, decays exponentially into the bulk and levels off at a value $\tilde{u}_D^*/\cosh(h/\ell)$. In turn, the MinD-ATP concentration increase from $\tilde{u}_T^*$ to $\tilde{u}_T^* + \tilde{u}_D^*[1 - 1/\cosh(h/\ell)]$, i.e. the ATP-form which is the one that can attach to the membrane is depleted close to the membrane. The latter suggest to call ℓ a 'recycling length' as it binds the active form of MinD (ATP-bound form) away from the membrane. The equilibrium values of the protein concentrations at the membrane, $\tilde{u}_D^*$, $\tilde{u}_T^*$, and u_m^*, are determined by the reactive boundary condition, Eq.(50a)-(50b), and the stationarity condition for the membrane dynamics, Eq.(49),

$$\frac{\ell_{\rm off}^2}{\ell}\, \tanh\left(\frac{h}{\ell}\right) = \frac{u_m^*}{\tilde{u}_D^*}\,, \tag{53a}$$

$$f_{\rm on}(u_m^*, \tilde{u}_T^*) = k_{\rm off}\, u_m^*\,, \tag{53b}$$

where we have defined the length scale $\ell_{\rm off} := \sqrt{D_c/k_{\rm off}}$, together with mass conservation,

$$\bar{n} = \tilde{u}_T^* + \tilde{u}_D^* + u_m^*/h\,, \tag{54}$$

where $\bar{n}$ represents the mean total mass density.

If the penetration depth is much smaller than the column height, $\ell \ll h$ (i.e. $h \to \infty$), Eq.(53a) this reduces to

$$\frac{\ell_{\rm off}^2}{\ell} = \frac{u_m^*}{\tilde{u}_D^*}\,. \tag{55}$$

Since the total mass density is an upper bound for the bulk densities, $\bar{n} > \tilde{u}_D$, this implies that the stationary membrane density u_m^* remains bound from above in the limit $h \to \infty$

$$\lim_{h\to\infty} u_m^* < \bar{n}\,\frac{\ell_{\text{off}}^2}{\ell} = \bar{n}\,\frac{\sqrt{D_c\lambda}}{k_{\text{off}}}\,. \tag{56}$$

Strikingly, despite the absence of an explicit saturation term, there is an *emergent* saturation effect for the membrane concentration. In addition, this saturation effect is due to the combined effect of detachment and nucleotide exchange but completely independent of the attachment dynamics (f_{on}) that can be highly nonlinear/cooperative. We conclude that if reattachment to the membrane requires reactivation (which is generic for many protein classes), e.g. in the form of a nucleotide exchange, then the stationary flux onto the membrane, $f_{\text{on}}(u_m, \tilde{u}_T) = k_{\text{off}}\, u_m$ is limited to the value $\sqrt{D_c\lambda}$. As an ancillary remark, the emergent saturation provides an explanation for the surprising observation that models with simplified (unsaturated) recruitment term $\propto k_{dD} u_d u_{DT}$ (as the skeleton model used here) reproduces the dynamics *in vivo* as well as *in-vitro* with essentially the same kinetic parameters despite the fact that membrane densities *in-vitro* are two orders of magnitude higher than *in vivo*.

The saturation effect strictly requires the extended bulk dimension. To see this consider the analogous set of reaction equations with reduced bulk dimension (as described in the previous section III B 1)

$$\partial_t \bar{u}_D(t) = k_{\text{off}}\, u_m/h - \lambda \bar{u}_D\,, \tag{57a}$$

$$\partial_t \bar{u}_T(t) = -f_{\text{on}}(u_m, \bar{u}_T)/h + \lambda \bar{u}_D \tag{57b}$$

$$\partial_t u_m(t) = f_{\text{on}}(u_m, \bar{u}_T) - k_{\text{off}}\, u_m\,, \tag{57c}$$

where $\bar{u}_i(t) = \frac{1}{h}\int_0^h \mathrm{d}z\, u_i(z,t)$ denotes the spatial average over the cytosolic densities. From Eq. (57a) with the left hand side set to zero we obtain for the stationary states

$$u_m^* = h\,\frac{\lambda}{k_{\text{off}}}\,\bar{u}_D^*\,. \tag{58}$$

For any finite $\bar{u}_D^*$, there is obviously no saturation in the limit $h \to \infty$, and

$$\lim_{h\to\infty} u_m^* = \infty\,. \tag{59}$$

This clearly shows that due to the nucleotide exchange process the reduction of the bulk dimension is not a valid approximation for large bulk heights. If, however, the bulk height is small compared to the reactivation length scale ($h \ll \ell$), then the hyperbolic tangent can approximated as $\tanh(h/\ell) \approx h/\ell$. In this limit the reactive boundary conditions, Eq. (50a) and (50b), for the stationary bulk profiles reduce to

$$D_c \nabla_z u_D|_{z=0} = \lambda \tilde{u}_D^* h = k_{\text{off}} u_m^*\,, \tag{60a}$$

$$D_c \nabla_z u_T|_{z=0} = -\lambda \tilde{u}_D^* h = -f_{\text{on}}(u_m^*, u_T^*)\,, \tag{60b}$$

which is equivalent to the stationarity condition in the reduced system obtained from Eqs. (57a) and (57b) by setting the left hand sides to zero.

We conclude that nucleotide exchange prohibits reduction of the bulk dimension unless $h \ll \ell$. For the Min system studied *in-vitro* one has $h/\ell = \mathcal{O}(10^3)$ [11], i.e. one is actually in the opposite limit $h \gg \ell$ where bulk dynamics is essential. Neglecting nucleotide exchange or reducing the bulk dimension if the condition $h \ll \ell$ is not met would be seriously flawed as it misses the saturation of membrane attachment. In large (*in-vitro*) systems this either necessitates the inclusion of explicit *ad hoc* saturation terms that perturb the nonlinear dynamics and introduce additional parameters, or it leads to membrane densities that exceed the carrying capacities of a membrane (due to volume exclusion) by orders of magnitude. Both of these 'quick fixes' are unsuitable for a quantitative theoretical account for reaction-diffusion systems.

C. Reduction to 2D slice geometry

Since the bulk dimension cannot be eliminated a reduction of the spatial dimension can only be sought on the membrane. Let us assume cartesian coordinates (x, y, z) with the membrane at $z = 0$. Let us further assume a spiral wave pattern at the membrane with the spiral centre at $x = y = 0$. On any coordinate axis (either $y = 0$ or $x = 0$) we now find for any protein density u_i an approximately constant density profile in the direction orthogonal to the axis under consideration, i.e. $\nabla_y u_i|_{y=0} \approx 0$ or $\nabla_x u_i|_{x=0} \approx 0$. By focusing on such a section of the system we loose the ability to distinguish between spiral wave patterns, target wave patterns, and travelling wave patterns, but we also reduce the reactive membrane to one dimension and the diffusive bulk to two dimensions. To study the mechanisms behind wave formation and coherence in general this is a very convenient reduction. Most importantly it allows us to run simulations on a time-scale of hours and days (2D) rather than weeks and months (3D). Therefore, we will perform the mechanistic analysis of wave dynamics in the 2D section and compare the results with a single representative 3D simulation that utilises the same parameters as the reduced 2D system. For now on we will refer to the reduced 2D system as the (x, z) frame, with the lateral dimension x and the extended bulk dimension z.

IV. LINEAR STABILITY ANALYSIS IN BOX GEOMETRY

The starting point of any linear stability analysis is the computation of a steady state around which the system can be linearised. For spatially extended systems this is typically a spatially uniform steady state. However, in the box geometry under consideration such a uniform steady state does not exist: While the steady state is spatially uniform along the membrane (in the lateral direction), nucleotide exchange in the bulk (longitudinal direction) induces density gradients characteristic for source-degradation processes; see also the discussion in the preceding section. Note that in general nonlinearities acting on non-uniform density profiles could seriously complicate the stability analysis due to mode-coupling. In the present case, however, the nonlinearities are restricted to the reactive boundary (membrane) such that the non-uniformity in the bulk (cytosol) has no direct effect on the nonlinear dynamics, i.e. it does not cause mode-coupling.

In the following we consider a 2D slice geometry as described above, with the lateral dimension x and the extended bulk (longitudinal) dimension z. A spatially uniform state at the membrane means that $\nabla_x u_i = 0$ for all protein densities. The stationary density profiles in the bulk are then given by (c.f. Sec. III B 2)

$$u_{DD}(z) = \tilde{u}^*_{DD} \frac{\cosh\left((h-z)/\ell\right)}{\cosh\left(h/\ell\right)}\,, \tag{61a}$$

$$u_{DT}(z) = \tilde{u}^*_{DT} + \tilde{u}^*_{DD}\left(1 - \frac{\cosh\left((h-z)/\ell\right)}{\cosh\left(h/\ell\right)}\right)\,, \tag{61b}$$

$$u_E(z) = \tilde{u}^*_E\,, \tag{61c}$$

where $\tilde{u}^*_i$ denote the spatially uniform stationary cytosolic densities at the membrane, and $\ell = \sqrt{D_c/\lambda}$ gives the penetration depth into the cytosol; note that the corresponding stationary profiles of the total mass densities, $u_E(z)$ and $u_D(z) = u_{DD}(z) + u_{DT}(z)$, are spatially uniform in the bulk. Upon inserting all these stationary bulk density profiles into the reactive boundary conditions at the membrane, Eqs. (31a)-(31c), one finds

$$\ell\,\tilde{u}^*_{DD}\,\tanh\left(h/\ell\right) = f_{DD}(u^*_{de})/\lambda\,, \tag{62a}$$

$$-\ell\,\tilde{u}^*_{DD}\,\tanh\left(h/\ell\right) = f_{DT}(\tilde{u}^*_{DT}, u^*_d)/\lambda\,, \tag{62b}$$

$$0 = f_E(\tilde{u}^*_E, u^*_d, u^*_{de})\,, \tag{62c}$$

which are complemented by the stationarity conditions for the membrane dynamics, Eq. (29d)-(29e),

$$0 = f_d(\tilde{u}^*_{DT}, \tilde{u}^*_E, u^*_d, u^*_{de})\,, \tag{63a}$$

$$0 = f_{de}(\tilde{u}^*_E, u^*_d, u^*_{de})\,. \tag{63b}$$

(As an aside we note that the above five equations determining the equilibria are not independent: $f_{de} = 0$ is the same condition as $f_E = 0$, and upon adding Eq. (63a) and Eq. (63b)

one finds $f_{DD} + f_{DT} = 0$, which is equivalent to $f_{de} = 0 = f_d$. Hence, there is no new information in the stationarity conditions on the membrane which is not already contained in the flux balance condition on the membrane.) Moreover, the stationary states have to satisfy global mass conservation

$$\overline{[\mathrm{MinD}]} = \tilde{u}^*_{DD} + \tilde{u}^*_{DT} + (u^*_d + u^*_{de})/h\,, \tag{64a}$$

$$\overline{[\mathrm{MinE}]} = \tilde{u}^*_E + u^*_{de}/h\,. \tag{64b}$$

In a linear stability analysis one considers the time evolution of small perturbations with respect to these stationary states, i.e. $u_i(x,z,t) = u^*_i(z) + \delta u_i(x,z,t)$ (where membrane densities lack the dependence on the z-coordinate). Expanding the dynamics of the small perturbations in terms of Fourier modes

$$\delta u_{DD}(x,z,t) = \sum_q e^{\sigma_q t} \cos(qx)\, \zeta_{DD}(z;q)\,, \tag{65a}$$

$$\delta u_{DT}(x,z,t) = \sum_q e^{\sigma_q t} \cos(qx)\, \zeta_{DT}(z;q)\,, \tag{65b}$$

$$\delta u_E(x,z,t) = \sum_q e^{\sigma_q t} \cos(qx)\, \zeta_E(z;q)\,, \tag{65c}$$

$$\delta u_d(x,t) = \sum_q e^{\sigma_q t} \cos(qx)\, \delta\tilde{u}^q_d\,, \tag{65d}$$

$$\delta u_{de}(x,t) = \sum_q e^{\sigma_q t} \cos(qx)\, \delta\tilde{u}^q_{de}\,, \tag{65e}$$

and inserting $u_i(x,z,t) = u^*_i(z) + \delta u_i(x,z,t)$ into the (linear) bulk diffusion equations (Eq. 29a-29c) and taking the boundary conditions (Eq. 31a-32c) into account, the corresponding bulk functions $\zeta_i(z;q)$ are obtained analytically as

$$\zeta_{DD}(z;q) = \delta\tilde{u}^q_{DD}\ \frac{\cosh\left(\frac{h-z}{\ell_q(\lambda+\sigma_q)}\right)}{\cosh\left(\frac{h}{\ell_q(\lambda+\sigma_q)}\right)}\,, \tag{66a}$$

$$\zeta_{DT}(z;q) = (\delta\tilde{u}^q_{DT} + \delta\tilde{u}^q_{DD})\ \frac{\cosh\left(\frac{h-z}{\ell_q(\sigma_q)}\right)}{\cosh\left(\frac{h}{\ell_q(\sigma_q)}\right)} - \delta\tilde{u}^q_{DD}\ \frac{\cosh\left(\frac{h-z}{\ell_q(\lambda+\sigma_q)}\right)}{\cosh\left(\frac{h}{\ell_q(\lambda+\sigma_q)}\right)}\,, \tag{66b}$$

$$\zeta_E(z;q) = \delta\tilde{u}^q_E\ \frac{\cosh\left(\frac{h-z}{\ell_q(\sigma_q)}\right)}{\cosh\left(\frac{h}{\ell_q(\sigma_q)}\right)}\,, \tag{66c}$$

where we have defined

$$\ell_q(\chi_q) := \sqrt{\frac{D_c}{\chi_q + D_c q^2}}\,, \tag{67}$$

generalising the penetration depth ℓ to a wave vector dependent quantity, and $\delta\tilde{u}^q_i$ are Fourier coefficients that depend on the wavenumber q.

Using the shorthand notation for a term describing the coupling between the membrane concentrations and the density profiles in the bulk

$$\Gamma_q(\chi_q) = \frac{D_c}{\ell_q(\chi_q)} \tanh\left(\frac{h}{\ell_q(\chi_q)}\right), \tag{68}$$

and the first Taylor coefficient for the reaction terms

$$f_j^i = \left.\frac{\partial f_j(\mathbf{u})}{\partial u_i}\right|_{\mathbf{u}=\mathbf{u}^*}, \tag{69}$$

the linear system reads $\mathcal{L}_q\,\delta\tilde{\mathbf{u}}_q = 0$, for each $\delta\tilde{\mathbf{u}}_q = \left[\delta\tilde{u}^q_{DD}, \delta\tilde{u}^q_{DT}, \delta\tilde{u}^q_E, \delta\tilde{u}^q_d, \delta\tilde{u}^q_{de}\right]^T$, where $\mathcal{L}_q$ is given by

$$\mathcal{L}_q = \begin{bmatrix} f^{DD}_{DD}-\Gamma_q(\sigma_q+\lambda) & f^{DT}_{DD} & f^{E}_{DD} & f^{d}_{DD} & f^{de}_{DD} \\ f^{DD}_{DT}+\Gamma_q(\sigma_q+\lambda)-\Gamma_q(\sigma_q) & f^{DT}_{DT}-\Gamma_q(\sigma_q) & f^{E}_{DT} & f^{d}_{DT} & f^{de}_{DT} \\ f^{DD}_{E} & f^{DT}_{E} & f^{E}_{E}-\Gamma_q(\sigma_q) & f^{d}_{E} & f^{de}_{E} \\ f^{DD}_{d} & f^{DT}_{d} & f^{E}_{d} & f^{d}_{d}-\sigma_q-D_m q^2 & f^{de}_{d} \\ f^{DD}_{de} & f^{DT}_{de} & f^{E}_{de} & f^{d}_{de} & f^{de}_{de}-\sigma_q-D_m q^2 \end{bmatrix}. \tag{70}$$

The first three rows of $\mathcal{L}_q$ are the linearisation of the reactive boundaries Eq. (31a)-(31c), and the last two rows are the linearisation of the membrane dynamics Eq. (29d)-(29e).

The dispersion relation $\max \mathrm{Re}[\sigma_q]$ (i.e. the fastest growth rates of each wavenumber q) are then obtained as solutions of

$$\det \mathcal{L}_q = 0\,. \tag{71}$$

Since $\mathcal{L}_q$ is non-algebraic in σ_q, solutions can only be obtained numerically. For this purpose we use the iterative solver `FindRoot[]` provided by Wolfram Mathematica 9 to compute the data shown in Fig. 2a,d and Fig. 4a,c in the main text.

V. NUMERICAL SIMULATION

All simulations have been performed with Comsol Multiphysics 4.4 that employs the finite element method. In all 2D simulations of the aforementioned (x, z) frame the system geometry is a rectangle with variable height h and fixed width $L = 500\mu m$. The boundaries $x = 0, L$ we employ periodic boundary conditions. We use a free triangular mesh with minimal mesh element size $\mathcal{M}_{\min} = 0.05\mu m$ at the membrane and a maximal mesh element size $\mathcal{M}_{\max} = 5\mu m$ in the bulk far away from the membrane. Close to the membrane the bulk mesh element size increases with a mesh growth rate r set to $r = 1.2$ (c.f. the documentation of Comsol Multiphysics for the details). All mesh sizes are chosen conservatively well below the smallest length scale of the observed pattern. Further reducing the mesh size has no effect on the simulation results. All simulations were performed using the direct PARDISO solver with relative tolerance manually set to 10^{-6} and default settings otherwise.

VI. EXTRACTING LOCAL EQUILIBRIA, AMPLITUDES AND CONTROL VARIABLES FROM NUMERICAL DATA

This chapter contains a description of the procedures we used to determine local equilibria, amplitudes and control variables from our numerical data.

A. Local membrane equilibria

In Section I we have introduced the 'Gedankenkonstrukt' (notional construct) of a local equilibrium for reaction-diffusion systems in a uniform d-dimensional reaction volume. Here we generalize this concept to situations where a reactive surface (membrane) is coupled to a bulk volume (cytosol).

Before giving a formal definition, let us take a step back and reiterate and expand on the main idea behind the local equilibrium concept. From the analysis of the planar 2-component reaction-diffusion system in Section I we have learned that any lateral instability (with unequal diffusion coefficients) induces a local change of total mass densities, and thereby shifts local equilibria. But what can be learned from the information about the local equilibria? One of the key advances brought about by the framework of nonlinear dynamics is the concept of *phase portraits*, which are geometric representation of the flow (system trajectories) in the phase space of a dynamical system. For well-mixed systems, already a calculation of the fixed points (equilibria) along with the surrounding flow field (linear stability) may often suffice to infer the global dynamics (attractors) of the system qualitatively. For instance, the dynamics in a system with one stable equilibrium will converge towards this stable state. In a system with two stable and one unstable equilibria, the unstable equilibrium will separate the basins of attraction of the two stable equilibria; as such the initial condition will fully determine the fate of the dynamics. If there is a single equilibrium which is oscillatory unstable (complex eigenvalues) the attractor approached by the dynamics is likely to be a limit cycle and the *structure of the flow field* (i.e. the topology of the associated vector field) that guides any dynamics will be that of a spiral with increasing amplitude (i.e. the distance to the unstable equilibrium). Of course, there are many more intricate cases that do not allow such a global a priori assessment of the flow flied in phase space (phase portrait). However, it is striking that a broad range of non-equilibrium phenomena can be reproduced and elucidated on the basis of such simple systems. Let us now illustrate how the notion of phase portraits is useful also for the investigation of spatially extended systems. One of the most prominent classical examples, is the complex Ginzburg-Landau equation, which exhibits wave solutions as well as states of spatio-temporal chaos. In this model system the local flow field has the generic structure of a stable limit cycle close to supercritical Hopf bifurcation (Stuard-Landau oscillators). In the complex Ginzburg-Landau equation these local dynamics are coupled diffusively, however, the local flow field in phase space is spatially uniform and invariant with respect to the system dynamics (i.e. there is no movement of equilibria). If we now imagine the

time-evolution of a spatially non-uniform state (e.g. a wave pattern) then all local dynamics will be guided by the flow field imposed by the Stuard-Landau oscillator. However, neighbouring points will be shifted in phase and diffusion will try to remove this difference. Therefore, the actual local trajectories of the spatially extended system will not be trajectories of the local dynamical system (Stuard-Landau oscillators) per se, and the stable limit cycle of the local dynamical system will never be reached (despite being the local attractor). We note this to emphasise that it is actually *not the local attractors which reflect the dynamics of the spatially extended system, but the flow fields they impose.* These flow fields can be inferred from a linear stability and bifurcation analysis of the local dynamical system.

With this in mind we can rephrase and specify the idea behind the notion of a local equilibrium: To infer local attractors from the observed spatiotemporal dynamics (in our case simulation data) in order to infer the structure of the local flow field (in local phase space) by computing the position, stability, and bifurcations of local equilibria as some control variables (local total densities) are varied.

Therefore, in the case of a reactive membrane coupled to a cytosolic volume, these local equilibria and attractors have to be defined such as to reflect the structure of the *instantaneous local flow field in local phase space* which guides the dynamics at a given membrane position $(x, y, z)|_{z=0}$ at time t. Consider a (two-dimensional) slice of the box geometry as described in Section III C and denote the membrane position by x. Since the reactive dynamics at the membrane is coupled to a cytosolic column of height h, one has to specify in the definition of local equilibria at the membrane (short: local membrane equilibria) how to account for the diffusive dynamics in the extended bulk direction. At first sight, one might argue that one should (for each membrane position x) integrate the instantaneous cytosolic densities over the whole cytosolic column $[0, h]$, and then compute the local equilibria (at position x) using the thereby obtained total masses. Such a definition would, however, in general not be useful for understanding the local reaction dynamics at the membrane at a given time t as it includes proteins far away from the membrane that do not participate in the reactive dynamics at that given time. Those proteins only have a delayed effect since they need to diffuse to the membrane before they can participate in any reaction (in addition, these proteins would also spread laterally).

Aiming for an *instantaneous local flow field in local phase space* one needs a definition of local membrane equilibria that only depends on the protein densities at the membrane. This includes the cytosolic densities at the membrane $\{\tilde{u}_{DD}(x,t),\, \tilde{u}_{DT}(x,t),\, \tilde{u}_{E}(x,t)\}$, as well as the densities on the membrane $\{u_d(x,t),\, u_{de}(x,t)\}$. Imagine now a situation where at some time t the cytosolic column is in diffusive equilibrium with the membrane (and hence the bulk profiles are the stationary profiles corresponding to the given protein densities at the membrane, c.f. Section III B 2). Then, there would be no net protein flux to and from the membrane due to cytosolic diffusion, i.e. no effect of the diffusive dynamics in the cytosol on the membrane dynamics. In this case only a change of the densities at the membrane would induce dynamics in the cytosol. As a consequence, the structure of the flow field in

local phase space would be completely determined by the densities at the membrane at time t and invariant with respect to diffusive dynamics in the cytosolic column. Moreover, the local values of the total mass densities controlling the ensuing equilibria and their stability would be those contained in the whole cytosolic column $[0, h]$.

All these statements would remain strictly valid as long as the bulk adiabatically follows the membrane dynamics (which in any realistic scenario is certainly not the case). However, for defining local membrane equilibria, it is key to realise that the local flow field which guides the local protein dynamics at the membrane is not determined by the globally conserved mass densities, but only by the local values of these mass densities right at the membrane. This suggests the following definition of a local membrane equilibrium: Given the protein densities at the membrane at some time t, one constructs the stationary density profiles in the bulk that correspond to these membrane densities; we call this an adiabatically extrapolated bulk. This ensures, as we have argued above, that the ensuing flow fields are independent of the diffusive cytosolic dynamics far away from the membrane at this particular time t. Hence, the local flow fields obtained from constructing the adiabatic bulk corresponding to a given set proteins densities at the membrane have precisely that property which one expects from a proper notion of local equilibrium: It reflects the flow field of the nonlinear dynamics at the membrane at time t.

It is important to realise that the total mass computed with the adiabatic bulk does not necessarily coincide with the total mass in the actual system, it only reflects the total mass that affects the nonlinear dynamics at time t. As we will see below, for the model of the Min system considered in this article the average mass in the adiabatic bulk does coincide with the actual mass in the cytosol system. As such, all spatial averages of densities computed with the adiabatic bulk remain conserved.

Next we will present the detailed computation of local equilibria from the simulations of the model for the Min system. We denote all densities extracted from simulations by a superscript and positions and times by subscripts $u_i^{\mathrm{num}}(x,t)$. With the total cytosolic MinD density $u_D = u_{DD} + u_{DT}$ the stationary bulk dynamics are obtained by solving the stationary diffusion equation

$$0 = D_D \nabla_z^2 u_D \,, \tag{72a}$$

$$0 = D_E \nabla_z^2 u_E \,, \tag{72b}$$

subject to reflective boundary conditions at the surface $z = h$

$$D_D \nabla_z u_D|_{z=h} = 0 \,, \tag{73a}$$

$$D_E \nabla_z u_E|_{z=h} = 0 \,, \tag{73b}$$

and fixed (Dirichlet) boundary conditions at the membrane

$$\tilde{u}_D = u_D|_{z=0} = u_{DD}^{\mathrm{num}}(x,t) + u_{DT}^{\mathrm{num}}(x,t) \,, \tag{74a}$$

$$\tilde{u}_E = u_E|_{z=0} = u_E^{\mathrm{num}}(x,t) \,. \tag{74b}$$

Since the solutions to theses equations are simply constant in space we obtain for the local total densities, $[\mathrm{MinD}]^{\mathrm{num}}_{x,t}$ and $[\mathrm{MinE}]^{\mathrm{num}}_{x,t}$, extracted from the simulations

$$[\mathrm{MinD}]^{\mathrm{num}}_{x,t} = u^{\mathrm{num}}_{DD}(x,t) + u^{\mathrm{num}}_{DT}(x,t) + \left[u^{\mathrm{num}}_{d}(x,t) + u^{\mathrm{num}}_{de}(x,t)\right]/h\,, \tag{75}$$

$$[\mathrm{MinE}]^{\mathrm{num}}_{x,t} = u^{\mathrm{num}}_{E}(x,t) + u^{\mathrm{num}}_{de}(x,t)/h\,. \tag{76}$$

The local equilibria are then obtained as shown in Section IV with the local total densities

$$[\mathrm{MinD}]^{\mathrm{num}}_{x,t} = u^{*\mathrm{num}}_{DD} + u^{*\mathrm{num}}_{DT} + (u^{*\mathrm{num}}_{d} + u^{*\mathrm{num}}_{de})/h \tag{77}$$

$$[\mathrm{MinE}]^{\mathrm{num}}_{x,t} = u^{*\mathrm{num}}_{E} + u^{*\mathrm{num}}_{de}/h. \tag{78}$$

As discussed above, we note that due to the assumption of an adiabatic bulk the (lateral) spatial averages denoted by an overbar are not identical in general, i.e. $\overline{[\mathrm{MinD}]}^{\mathrm{num}}_{x,t} \neq \overline{[\mathrm{MinD}]}_x$ and $\overline{[\mathrm{MinE}]}^{\mathrm{num}}_{x,t} \neq \overline{[\mathrm{MinE}]}_x$. However, we find that the deviation is small and maximal in the turbulent state ($h = 20\mu m$):

$$\left(\overline{[\mathrm{MinD}]}^{\mathrm{num}}_{x,t} - \overline{[\mathrm{MinD}]}_x\right)/\overline{[\mathrm{MinD}]}_x \leq 0.01 \tag{79}$$

$$\left(\overline{[\mathrm{MinE}]}^{\mathrm{num}}_{x,t} - \overline{[\mathrm{MinE}]}_x\right)/\overline{[\mathrm{MinE}]}_x \leq 0.02. \tag{80}$$

These error bounds are one order of magnitude smaller for globally coherent traveling wave pattern observed at $h > 33\mu m$. The stability of local equilibria can be computed for the data extracted from simulations at any point x and time t as shown in Section IV by setting $q = 0$ and using $[\mathrm{MinD}]^{\mathrm{num}}_{x,t}$ and $[\mathrm{MinE}]^{\mathrm{num}}_{x,t}$ as total densities.

B. Control variables Σ and Δ

By our definition control variables are the local values of globally conserved quantities (total mass densities). We are mainly interested in the local change of these control variables relative to their globally conserved average. Hence, we normalise the total mass densities to the global averages

$$D_{x,t} = [\mathrm{MinD}]^{\mathrm{num}}_{x,t}/\overline{[\mathrm{MinD}]} \tag{81}$$

$$E_{x,t} = [\mathrm{MinE}]^{\mathrm{num}}_{x,t}/\overline{[\mathrm{MinE}]}. \tag{82}$$

Min protein oscillations are driven by the cyclic alternation between MinD dominance (accumulation at the membrane) and MinE dominance (depletion of the membrane). This dominance can only alternate by changing local densities. Therefore, the local ratio of MinE and MinD represents a natural control parameter for the dynamics, we define

$$\Delta_{x,t} = E_{x,t}/D_{x,t} \tag{83}$$

Since the cytosol is adiabatically slaved to the membrane dynamics on average, i.e.

$$\overline{[\mathrm{MinD}]}^{\mathrm{num}}_{x,t} \approx \overline{[\mathrm{MinD}]}_x, \tag{84}$$

$$\overline{[\mathrm{MinE}]}^{\mathrm{num}}_{x,t} \approx \overline{[\mathrm{MinE}]}_x, \tag{85}$$

the values of $\Delta_{x,t}$ remain centered around the ratio of the global average

$$\Delta_0 = \overline{E}_{x,t}/\overline{D}_{x,t}. \tag{86}$$

For the second control variable we choose the orthogonal coordinate which is a measure for the relative change of the joined total mass of MinD and MinE

$$\Sigma_{x,t} = \sqrt{\frac{1}{2}(E^2_{x,t} + D^2_{x,t})}, \tag{87}$$

and analogously the global average

$$\Sigma_0 = \sqrt{\frac{1}{2}(\overline{E}^2_{x,t} + \overline{D}^2_{x,t})}. \tag{88}$$

A representation of the coordinates in control space is shown in Supplementary Fig. 3.

C. Amplitudes

To simplify summation over components of the species MinD and MinE we define the index sets for MinD

$$\mathcal{D} = \{DD, DT, d, de\} \tag{89}$$

and for MinE

$$\mathcal{E} = \{E, de\}, \tag{90}$$

as well as the coefficient

$$\gamma_i = \begin{cases} 1/h^2 & \text{if } i \in \{d, de\} \text{ (surface densities)} \\ 1 & \text{if } i \in \{DD, DT, E\} \text{ (volume densities)} \end{cases} \tag{91}$$

to homogenise the dimensions.

We define the local amplitude of the pattern $A_{\mathrm{pattern}}(x,t)$:

$$A^2_{\mathrm{pattern}}(x,t) = \left(\frac{\sqrt{\sum_{i\in\mathcal{D}} \gamma_i \left(u_i^{\mathrm{num}} - \bar{u}_i^{\mathrm{num}}\right)^2}}{\sqrt{\sum_{i\in\mathcal{D}} \gamma_i \left(\bar{u}_i^{\mathrm{num}}\right)^2}} \right)^2 + \left(\frac{\sqrt{\sum_{i\in\mathcal{E}} \gamma_i \left(u_i^{\mathrm{num}} - \bar{u}_i^{\mathrm{num}}\right)^2}}{\sqrt{\sum_{i\in\mathcal{E}} \gamma_i \left(\bar{u}_i^{\mathrm{num}}\right)^2}} \right)^2 \tag{92}$$

the local distance from the local equilibrium $A_{\mathrm{stat}}(x,t)$:

$$A^2_{\mathrm{stat}}(x,t) = \left(\frac{\sqrt{\sum_{i\in\mathcal{D}} \gamma_i \left(u_i^{\mathrm{num}} - u_i^{*\mathrm{num}}\right)^2}}{\sqrt{\sum_{i\in\mathcal{D}} \gamma_i \left(u_i^{*\mathrm{num}}\right)^2}} \right)^2 + \left(\frac{\sqrt{\sum_{i\in\mathcal{E}} \gamma_i \left(u_i^{\mathrm{num}} - u_i^{*\mathrm{num}}\right)^2}}{\sqrt{\sum_{i\in\mathcal{E}} \gamma_i \left(u_i^{*\mathrm{num}}\right)^2}} \right)^2 \tag{93}$$

and the amplitude in control space $A_{\text{control}}(x,t)$:

$$A^2_{\text{control}}(x,t) = (\Sigma_{x,t} - 1)^2 + (\Delta_{x,t} - 1)^2 \ . \tag{94}$$

Note that $\Sigma_{x,t}$ and $\Delta_{x,t}$ are defined with respect to the normalised densities D and E.

VII. MAINTENANCE OF CHEMICAL TURBULENCE BELOW THE ONSET OF THE TURING INSTABILITY

To test whether a lateral instability of the spatially uniform state is required for the maintenance of chemical turbulence we modified the bulk equation of MinE (Eq. 29c) such that the total MinE density in the system slowly degrades

$$\partial_t u_E = D_c \nabla_c^2 u_E - \mu_- u_E \,. \tag{95}$$

The degradation rate μ_- is set such that the induced gradients of size $\ell_- = \sqrt{D_c/\mu_-}$ at the membrane are negligible, i.e. $h \ll \ell_-$ (c.f. section III B 2). As initial condition for the simulation with slow bulk degradation we import a numerical solution at a specific time after the system became tubulent. In this case we picked the time index $t = 1.7 \cdot 10^4\, s$. With this initial condition we then start a new simulation with bulk degradation, where we used the degradation rate $\mu_- = 1 \cdot 10^{-3}\, s^{-1}$. This choice ensures that the penetration depth is negligible, i.e. $h/\ell_- = 0.08$.

We ran this simulation for $1.7 \cdot 10^3\, s$ after which the total Min density and the MinE/MinD ratio reduced to the values $\Sigma = 0.96$ and $\Delta = 0.91$, respectively. Although these values were well below the critical values $(\Sigma, \Delta) = (1, 1)$ for the onset of the lateral instability (c.f. Fig. 2d in the main text), the turbulent state remained phenomenologically unaltered during the whole simulation time, c.f. Supplementary Fig. 4. This shows that the lateral instability is subcritical and that linear instability of the uniform state is not required for chemical turbulence. In other words: **The lateral instability is a route to chemical turbulence, but not the origin.**

VIII. POINT-TO-POINT CORRELATION KYMOGRAPHS

To visually inspect the spatiotemporal dynamics of pattern-forming systems kymographs of the particle densities are typically used. In the present case the system size is very large compared to the smallest intrinsic spatial structure of the pattern (e.g. nonlinear wave profiles), which makes kymographs of the densities ill-suited for visual inspection. We are mainly concerned with the distinction between turbulent phases of the dynamics, standing wave patterns, and travelling wave patterns. In particular, we are interested in transition between these phases. The structure of the pattern on the smallest length scales is secondary.

For an oscillatory system, the spatial correlations between histories at different points in space reveal information about the spatial coherence of the pattern. We will, therefore, compare the histories of membrane densities at specific time points t and compute the correlation of spatially nearby membrane signals. This will yield *point-to-point correlation kymographs* which are defined as follows: The spatial domain of length $L = 500\,\mu m$ is discretised into bins with a spatial resolution of $\Delta x = 0.2\,\mu m$; the position of these bins reads $x_i = i\,\Delta x$ with i an integer. For a given time t, we record at each position x_i the membrane signal (here the overall MinD membrane density $u_d^{\rm tot} := u_d + u_{de}$)) over a time interval $T = 10\,s$ with a temporal resolution of $\Delta t = 1\,s$

$$m_i^T(t) = \left[u_d^{\rm tot}(x_i, t-T),\, \ldots\,,\, u_d^{\rm tot}(x_i, t-\Delta t),\, u_d^{\rm tot}(x_i, t)\right]. \tag{96}$$

We then, for each time point t, compute the Pearson correlation coefficients

$$\rho[m_i^T(t), m_{i\pm1}^T(t)] = \frac{\left\langle \left[m_i^T(t) - \left\langle m_i^T(t)\right\rangle\right] \cdot \left[m_{i\pm1}^T(t) - \left\langle m_{i\pm1}^T(t)\right\rangle\right]\right\rangle}{\sqrt{\left\langle \left[m_i^T(t) - \langle m_i^T(t)\rangle\right]^2\right\rangle}\,\sqrt{\left\langle \left[m_{i\pm1}^T(t) - \left\langle m_{i\pm1}^T\right\rangle(t)\right]^2\right\rangle}} \tag{97}$$

between membrane signals of neighbouring sites; here $\langle\cdot\rangle$ denotes the temporal mean, i.e. an average over the time sequence. Next, for each point x_i in space, we define what we term *local point-to-point correlation*

$$\rho_i^T(t) := \frac{1}{2}\Big(\,\rho[m_i^T(t), m_{i-1}^T(t) + \rho[m_i^T(t), m_{i+1}^T(t)]\,\Big), \tag{98}$$

where we assume periodic boundaries. This point-to-point correlations are then plotted as kymographs; see main text Figs. 3c, 5c, and Supplementary Fig. 9.

Since Δx is chosen much smaller that the characteristic length scales of the pattern, the point-to-point correlation will be typically high, i.e. $\rho_i^T \approx 1$. However, for any wave pattern with standing wave characteristic (which are at least transiently maintained on the timescale T), there will be wave nodes where the local variation of the signal is small compared to the variation of signals in the vicinity of the node. Accordingly, at these points the point-to-point correlation will be very small, i.e. $\rho_k^T \approx 0$.

The point-to-point correlations function provides kymographs with a high contrast between spatial domains of high and low point-to-point correlations, and thereby gives high-resolution information on the spatiotemporal evolution of wave node positions and distances

of wave nodes. For instance, standing wave patterns can be clearly identified by the uniform separation of spatially fixed wave nodes, c.f. main text Fig. 5 and Supplementary Fig. 9. Bands of travelling waves emitted from a source defect are identified as broad spatial domains of uniformly high point-to-point correlation which surrounds the two wave nodes of the source defect (single standing wave), c.f. main text Fig. 5. In the turbulent regime we observe spontaneous formations of wavefronts at (seemingly) random position, that drift in random directions with randomly varying velocities, and vanish spontaneously after random times, c.f. main text Fig. 3. A detailed analysis of the turbulent phase close to the transition to standing wave order will be made below in the following Supplementary section.

IX. TRANSITION FROM CHEMICAL TURBULENCE TO GLOBALLY COHERENT STANDING WAVES

In this section we provide the numerical evidence that the transition from chemical turbulence to coherent standing wave patterns is facilitated by the activation and interplay of two mutually commensurable modes induced by the lateral instability.

A. The defect control mode q_c

We start the discussion with the role of the *defect control mode* with wave vector q_c, which is the fastest growing mode within the band of linearly unstable modes. As described in the main text, its role is *the spatiotemporal coordination of local destabilisation, which results in the timed formation of finite sized and uniformly separated clusters of oscillatory unstable equilibria.*

To test this assertion we traced the temporal evolution of local stability in our numerical simulations: At every point x on the reactive membrane we extracted the local protein densities from the numerical data, and computed the stability of the respective local equilibria as described in the previous Sections VI A and IV of this Supplementary Material. Since we were primarily interested in their destabilisation we assigned a binary value to each local equilibrium, 0 for a stable equilibrium, and 1 for an unstable equilibrium. We extracted data from our simulations with a spatial resolution of $\Delta x = 0.4\,\mu m$ and a temporal resolution of $\Delta t = 1\,s$. We ran the simulations sufficiently long for the dynamics to enter a "stationary" phase, i.e. the spatiotemporal patterns to remain qualitatively unchanged for a sufficiently long time, here for about $\mathcal{O}(10^2)$-$\mathcal{O}(10^3)$ oscillation cycles (i.e. the spatial average of the local oscillation periods at each point in space x). From this "stationary" window we extracted the last $500s$ ($T = 500\,s$) corresponding to about $\mathcal{O}(10^1)$-$\mathcal{O}(10^2)$ local cycles. In this extracted window we computed the stability of local equilibria. Thereby we obtained, for every point x on our spatial grid, a binary sequence (string of 0s and 1s), $\mathbf{s}(x) = \{s_i(x)\}$, of length $T/\Delta t = 500$, encoding the time evolution of local stability change.

If the formation of defects is spatiotemporally coordinated, the local change of stability must be spatially correlated. To test defect coordination we, therefore, first computed the Pearson correlation coefficient $\rho(x_1, x_2) := \rho[\mathbf{s}(x_1), \mathbf{s}(x_2)]$ (c.f. Eq. (97)) for each pair of time sequences at space points x_1 and x_2 on our spatial grid. We then defined the spatial correlation function $C(r)$ characterising the local stability change,

$$C(r) = \overline{\rho(x_1, x_2)}|_{|x_1 - x_2| = r}\,, \tag{99}$$

where the average is taken over all pairs of space points (x_1, x_2) with given fixed distance $|x_1 - x_2| = r$. Since we were interested how the spatial correlation of the local equilibria's stability depends on the length scale $l_c = 2\pi/q_c$, set by the fastest growing mode q_c, we rescaled the spatial dimension by l_c and defined the dimensionless quantity $\tilde{r} := r/l_c$. To compare the spatial correlation for different system heights (control parameters) h we fitted

an envelope $G(\tilde{r})$ to all rescaled correlations functions $C(\tilde{r})$,

$$G(\tilde{r}) = \left(1 + \tilde{r}/\tilde{\xi}\right)^{-2}, \tag{100}$$

where $\tilde{\xi} := \xi/l_c$ serves as a measure for the correlation length in units of l_c. The correlation functions with corresponding envelopes are shown for a large set of control parameters h in Supplementary Fig. 5. Please note that the wave length of the fastest growing mode, l_c, depends on the value of the control parameter, here the system height, $l_c = l_c(h)$.

From these data we make two key observations: (i) First, the correlation functions oscillate spatially with a period set by the wave length of the fastest growing mode, l_c. This shows that local destabilisation of equilibria is controlled by the fastest growing mode q_c. (ii) Second, the correlation length ξ is effectively zero for $h \leq 23\,\mu m$ (in the turbulent regime), and increases monotonically to finite values $\xi > l_c$ for $h \geq 24\,\mu m$, i.e. as soon as the first mode $q_r = 2q_c$ that is commensurable with q_c becomes part of the band of unstable modes and thereby active (Supplementary Fig. 6, c.f. main text Fig. 4d). This indicates that as soon as it becomes unstable the commensurable mode q_r plays a key role in maintaining controlled local destabilisations at distances l_c. We will discuss this role and its consequences for the spatiotemporal dynamics in the following section.

B. The mass redistribution mode q_r

In the main text we argued that the concurrence of the transition from chemical turbulence to standing waves with the activation of the commensurable mode q_r is *not* a coincidence, but that commensurability of q_r with the wave vector of the fastest growing mode q_c is in fact the mechanism underlying the emergence of order. Key to the argument was that the q_r-mode is responsible for mass transport and determines the positions (distance from the source defect) where wavefronts are formed that are being send out by the source defects (which, in turn, are controlled by the q_c-mode). As a reminder: Source and sink defects can only be periodically formed at fixed positions if the mode responsible for mass transport is commensurable with the mode that coordinates defect distances (c.f. main text Fig. 4d and the corresponding section in the main text).

To consolidate this scenario, we inferred the characteristic distances of mass transport from the simulation data. Since mass transport is responsible for the destabilisation of local equilibria it must also be the cause for the redistribution of instability clusters (spatially connected sets of nearby unstable equilibria) from depleting source defects to nearby (propagating) wavefronts. Therefore, we can take the distance between instability clusters as a reliable and easyly accessible measure for the distance of mass transport.

Consider now a standing wave pattern (c.f. main text Fig. 4c,d), and let's take a closer look at the distances between instability clusters. From the wave profiles we infer three distinct distances between instability clusters (, c.f. Supplementary Figure 7):

(i) First, we observe short distances between shrinking instability clusters, corresponding to source defects, and instability clusters, belonging to wavefronts emitted by source defects.

Let us denote this length scale as the source-wavefront (sw) distance d_{sw}. (ii) Second, we observe large, temporally increasing distances, $d_{\mathrm{w+}}$, that correspond to nearby wavefronts that originated from the same source and are propagating away from each other. These distances between instability clusters are found once the source is fully depleted, and all local equilibria at the source position become stable, such that no instability clusters are left between the wavefronts emitted by the source. As those wavefronts propagate away from each other, $d_{\mathrm{w+}}$ is bound from below by twice the distance between source and wavefront, $2d_{\mathrm{sw}} \leq d_{\mathrm{w+}}$. (iii) Third, we observe intermediate, temporally decreasing distances, $d_{\mathrm{w-}}$, that correspond to wavefronts emitted by neighbouring sources, and, therefore, propagate towards each other. This distance continuously shrinks until the instability clusters (wavefronts) merge. Since sources are separated at uniform distances l_c, this distance $d_{\mathrm{w-}}$ is bound from above by $d_{\mathrm{w-}} < l_c - 2d_{\mathrm{sw}}$.

To check whether these distances are characteristic length scales of the spatiotemporal dynamics in the standing wave regime, we computed the statistical distribution of the distances between instability clusters, d_{ic}. These distances were extracted from the same data as the spatial correlations in the previous section (i.e. stationary phases of the pattern, $T = 500\ s$, $\Delta t = 1\ s$). In the standing wave regime ($24\ \mu m \leq h \leq 32\ \mu m$), all cluster distance distributions have a characteristic bimodal shape (Supplementary Fig. 7, c.f. main text Fig. 4d). Normalising the cluster distances d_{ic} to the respective length scale $l_r = 2\pi/q_r$, set by the commensurable mode q_r, shows that the first peak of the bimodal distribution exhibits a maximum around $l_r/2$, and extends to l_r, while the second peak of the distribution is bound from below by l_r.

From the foregoing observation of cluster distances in the standing wave profile we know that there are two bound distances, $d_{\mathrm{w+}}$ and $d_{\mathrm{w-}}$. The distance $d_{\mathrm{w-}}$, corresponding to merging wavefronts, is bound from above. Hence, these distances are entirely accumulated in the first peak of the distribution shown in Supplementary Fig. 7. On the other hand, the distance $d_{\mathrm{w+}}$ is bound from below since it corresponds to wavefronts propagating away from each other. Therefore, the distances $d_{\mathrm{w+}}$ must be entirely accumulated in the second peak of the cluster distribution. Moreover, since $d_{\mathrm{w+}}$ is bound from below by the distance of cluster redistribution d_{sw}, i.e. $2d_{\mathrm{sw}} \leq d_{\mathrm{w+}}$, our data reveals that this bound is set by l_r and we can identify $d_{\mathrm{sw}} \approx l_r/2$. In other words, the maximum of the first peak of the cluster distribution accumulates the source-wavefront distances d_{sw}, and this distance is set by the commensurable mass redistribution mode q_r in the standing wave regime.

Overall, the separation and sharpness of the two peaks in the cluster distance distribution can be seen as a measure for the precision with which the distance of mass transport (i.e. redistribution of instability clusters) is controlled. Upon comparing the instability cluster distance distributions of the standing wave regime and turbulent phase (e.g. at $h = 20\ \mu m$), the following features become apparent: In the turbulent phase (i) the distribution becomes much broader, (ii) the first peak gains weight and its maximum shifts towards zero, (iii) the separation between the two peaks becomes much weaker, and (iv) the alignment with the commensurable mode q_r is lost in the first peak. Hence, in the turbulent phase mass transport (redistribution of unstable clusters) takes place on a broad range of length scales.

Strikingly, full separation between both peaks in the cluster distribution occurs between $h = 23\,\mu m$ and $h = 24\,\mu m$, i.e. right as the commensurable mode q_r becomes active (unstable).

Taken together, we conclude that mass transport (redistribution of instability clusters) is controlled by the active commensurable mode q_r, otherwise (when q_r is not active) there is no robust length scale of mass redistribution.

C. Commensurability and interaction of mass redistribution and defect coordination modes: Predictions

So far we have made the following key observations when the system height (control parameter) h is increased above a threshold value $h \approx 23.5\,\mu m$ where an unstable mode q_r emerges which is commensurable with the fastest growing mode $q_r = 2q_c$:

- Instead of the (turbulent) pattern we observe spatially coherent standing waves with a characteristic wavelength set by the fastest growing mode: $l_c = 2\pi/q_c$.
- Changes in the stability of local equilibria become spatially correlated, and the corresponding correlation length ξ increases monotonously with the system height (control parameter) h.
- The correlation function for the stability of local equilibria oscillates spatially with a period set by the fastest growing mode q_c.
- A fixed length scale $l_r/2$ for mass transport (redistribution of instability clusters) is established by the active (unstable) commensurable mode $q_r = 2q_c$.

In the main text we argued that these observations are caused by the concerted interplay between the two commensurable modes q_c and $q_r = 2q_c$: If source defects are synchronously formed at a uniform distance, and if the emission of mass by these source defects (wavefront formation) is symmetric and synchronised in all directions, then the positions of source and sink defects are invariant. Based on this *mode commensurability mechanism*, one can make predictions for the dynamics in the turbulent phase close to the transition to the standing wave phase, where defect coordination and mass transport are almost commensurable. These predictions can then be compared with our numerical data and provide a critical test for the proposed mode commensurability mechanism for the emergence of standing wave patterns.

Assuming that robust defect coordination and mass transport are indeed caused by the interaction of the commensurable modes q_c and q_r, what can we infer about the phenomenology at the transition? Let us perform the following "Gedankenexperiment" (thought experiment): Assume that the mode $q_{\max}$ at the outmost right of the band of unstable modes, i.e. the unstable mode with the shortest wavelength $l_{\min} = 2\pi/q_{\max}$, is almost commensurable with the fastest growing mode q_c such that $2\pi/(l_{\min} - \delta) = 2q_c$ with some small $\delta > 0$.

Suppose that we align the troughs (the minima of the *defect control mode* which represent source defects where mass is redistributed from the minima to the maxima of the *mass redistribution mode*, c.f. main text Fig. 4d) of the modes q_c and $q_{\max}$ at some point in space. Henceforth, we will refer to this point as the *interface*); see Supp. Fig. 8 for an illustration. Then, at the right and left nearest neighbouring crests of the control mode (q_c), the mass redistribution mode ($q_{\max}$) has a phase shift of $+\delta$ and $-\delta$ with respect to the control mode, respectively. At the next neighbouring crests, this phase shift is $\pm 2\delta$, and it accumulates further as one moves away from the point of alignment (interface) until it reaches a full period $\pm 2\pi$ (phase slip) at some distance from the interface. Imagine now that an initial state given by a standing wave train of n wave nodes to the right and left to the interface respectively, and, for specificity, let's consider the left hand side of the interface. How does the concerted action of the control mode and the mass distribution mode now play out?

While the depleting mass sources, controlled by the q_c-mode, are still redistributed by the action of the mass redistribution mode $q_{\max}$, incommensurability between these modes implies that the left-right symmetry of mass redistribution is broken within each wave period of the control mode (c.f. Remark [12]). Wavefronts emitted by neighbouring sources do no longer merge (in a sink defect) in the exact center between the emitting sources, but at some off-center position which is half-way between the wavefronts at the crest of the mass-redistribution mode; for an illustration see again Supp. Fig. 8. We can expect that the phase shift between defect control and mass redistribution modes induces an increasing frustration with the distance from the interface that will at some point impede the concerted interplay between these two modes, and that this point will be reached well before the modes get out of phase at $n\delta = l_c/2$. As a consequence, the standing wave will be a finite wave packet with $k \ll l_c/(2\delta)$ nodes. After a half time period of the defect control mode the phase of the defect control mode will be shifted with respect to the mass redistribution mode by $\delta/2$ at the position of the first source defect left of the interface, $3\delta/2$ at the second source defect up to $(2k-1)\delta/2$ at the k-th defect to the left. Hence, in a band of k wave (space) periods the phase shift will have increased at each node by $\delta/2$ within a half time period (source-sink defect cycle), further increasing the frustration caused by the phase shift throughout the band of k waves. To maintain the wave form the positions of defects need to shift to the left – along with the controlling mode q_c. The increased frustration can be removed entirely at one side of the interface (here the left side) by shifting the defect control mode $\delta/2$ to the left each half period. Assuming that the phase shift is small enough at the k-th node to maintain the standing wave pattern, a shift of the defect control mode by δ to the left per cycle would maintain a constant phase shift at each wave node, and thereby the pattern. However, this would also shift the position of the interface by $\sim 2l_{\min} \approx l_c$ to the left with each cycle, whereas the wave nodes are only shifted by $\sim \delta$ to the left with each cycle. Given that $\delta \ll l_c$ for weak incommensurability this suggests that with each cycle a wave node is lost at the right hand side of the pattern as it slips behind the interface whereas an additional wave node can be maintained at the left hand side, overall maintaining a band of k wave nodes.

Since we have, for specificity, assumed that mass distribution leads to realignment of

the wave nodes for the control and mass distribution mode to the left of the interface, this concomitantly leads to an increasing misalignment to the right of the interface, as can be easily inferred from Supp. Fig. 8. The accumulating phase shift then quickly leads to phase slips at some constant distance from the interface. As the interface moves, these phase slips should, therefore, move alongside at a constant distance from the interface. In other words, while the wave train of k nodes to the left of the interface remains at some finite length is maintained, the pattern at the right of the interface is constantly broken up into smaller wave trains by those periodically generated phase slips.

Since the same arguments apply if we had assumed that the realignment of the wave combs happens to the right of the interface, one should observe interface propagation with the features of right and left propagating wave trains reversed. The choice between left and right will presumably depend on the history of the system.

Taken together, we predict – based on the hypothesis that order (global coherence) emerges due to commensurable mode interaction – the following precursor phenomena in the turbulent regime close below the threshold to the standing wave pattern regime:

(1) Alignment between the incommensurable wave modes q_r and q_c will lead to interfaces between left and right propagating wave trains. The speed of these interfaces v_I will be of the order of $v_I \approx l_c/\tau$, where τ denotes the period of one oscillation cycle. However, the above line of arguments suggests that the wave trains on both sides of the interface try to achieve alignment of the control modes to minimise the frustration caused by the phase shift on their respective sides. One may, therefore, expect that the realignment to the side where the wave train is maintained is hampered by the realignment the wave trains on the other side try to achieve. Hence, the estimate of the interface speed, which took only one side of the interface into consideration, is likely to be an upper bound, i.e. $v_I \lessapprox l_c/\tau$.

(2) In addition, we can also estimate the speed of the propagating train of standing waves v_W to be of the order of $v_W \gtrapprox \delta/\tau$, which is the minimal phase shift per period required to maintain the wave pattern.

(3) The two points above imply that the speed of the interface is much faster than the speed of the wave train, $v_I \gg v_W$. This means that during each oscillation cycle the (rightmost) wave at the interface slips behind the interface, thereby, dropping out of the wave train. At the same time the phase shift left to the wave train is reduced, enabling an additional wave node to join the wave train.

(4) The maintenance of wave nodes in the wave train should be more stable close to the interface where the phase shift between defect control and mass redistribution mode is minimal.

(5) There will be a preferred formation of extended propagating wave packets close to one side of the interface, and turbulent-like dynamics at the other side. More precisely, the wave trains emerging on the other side of the interface are short because of phase slips

induced by the moving interface. These phase slips should have a constant distance from the moving interface.

In the following section we will compare these predictions with the simulation data.

D. Commensurability and interaction of mass redistribution and defect coordination modes: Comparison with the simulation data

Supplementary Fig. 9 shows the point-to-point correlation kymograph for the case where q_c and $q_{\max}$ are weakly incommensurable ($\delta/l_c = 0.03$ for a control parameter $h = 23\,\mu m$) in the turbulent regime. Indeed, visual inspection of the kymograph does confirm our predictions: In the observed time window we find a standing wave train comprising a few ($\approx 5 \pm 2$) wave nodes drifting to the left. The right boundary of the wave packet marks a moving interface to right moving wave trains. As predicted, the maintenance of drifting wave nodes is most stable (i.e. the position of the wave node changes continuously without any interruptions) close to the interface where the phase shifts δ have not given rise to a phase slip. As soon as phase slips occur (visible as irregular interruptions of wave nodes) the pattern become more turbulent , such that the left boundary of the standing wave train cannot be well defined. On the right hand side of the interface (the right boundary of the standing wave train), wave nodes mainly drift to the right, but are often interrupted and reformed at an approximately constant distance nearby the interface.

All these observations are fully consistent with the above predictions based on our idealised Gedankenexperiment. To test the predictions also quantitatively we extracted the speed of the interface v_I and the speed of few wave trains v_W from the kymograph in Supplementary Fig. 9. We estimated the local oscillation period $\tau \approx 16.67\,s$ by averaging over several local oscillation periods. For the speed of the interface we find $v_I \approx 0.42\,\mu m/s < l_c/\tau \approx 0.77\,\mu m/s$, which, given the idealised nature of our estimate is a surprisingly good agreement (note that we expected the actual interface speed to be slower due to the influence of counter-propagating waves). For the speed of wave trains v_W we find values in the range $0.026\,\mu m/s \; - \; 0.069\,\mu m/s$, which is also consistent with our estimate of the lower bound $v_W \gtrsim \delta/\tau \approx 0.023\,\mu m/s$. Hence, the spatial structure of the turbulent state closely below threshold is not only fully consistent with our *commensurability mechanism*, but it even enables us to infer qualitative and quantitative details of precursor phenomena close to the transition from the turbulent to the standing wave phase from the assumption that order emerges from the control of local stability by two commensurable modes.

We will next discuss the spatiotemporal dynamics for a control parameter value, $h = 24\,\mu m$, which is slightly above the threshold for the activation of the commensurable mode q_r. Visual inspection of the point-to-point correlation kymograph shows that wave nodes are now maintained (in time) throughout the whole spatial domain. Strikingly, we also observe considerable drift of wave nodes in some parts of the spatial domain, as well as local defects (phase slips) of the spatial structure. We can identify interfaces between right- and left-moving wave trains similar to those found in the turbulent regime (for the control parameter

$h = 23\,\mu m$). In the particular time window shown in Supp. Fig. 9, there are several locations (interfaces) where the propagation direction of wave trains change. If this happens, the wave trains start to move apart from each other. The corresponding kymograph (Supp. Fig. 9) shows that the distance between the two wave nodes neighbouring the interface on the left and right start to increase. However, according to our notion that the pattern (which is comprises all wave trains) is controlled by two global (extending through the whole spatial domain) modes q_c and q_r, c.f. Supp. Fig 8 and main text Fig 4d, the observed divergence of wave nodes cannot proceed. If we assume that the modes maintain alignment with the wave train in one direction (say with the right propagating wave train), then the phase difference with the wave train propagating in the other direction will increase, leading to a phase slip at some point. In this case both wave trains will merge following the phase slip and maintain the drift in one direction. Alternatively, if neither wave train achieves alignment with the control modes, the phase difference will increase for the wave trains propagating in both directions and both will undergo a phase slip defect at some point. In this case both wave trains will also merge following the phase slip. These two possibilities are exactly what we observe in the kymograph. For both cases we can summarise that the global dynamics (the pattern) follow the control modes (trying to achieve alignment with them).

Increasing the control parameter h even further ($h \geq 25\,\mu m$) shows that the propagation of wave trains is reduced and the point-to-point correlation kymographs show increasing global coherence, which is consistent with the increasing correlation length of local stability change (c.f. Supp. Fig. 6).

E. Commensurability and interaction of mass redistribution and defect coordination modes: Conclusion and Summary

One main finding of our article is that the relevant part of the pattern forming dynamics in mass-conserved reaction-diffusion systems is the redistribution of total mass by unstable modes activated in a lateral instability. We were able to show analytically that unstable modes always induce a redistribution of total mass for unequal diffusion constants. Hence, it remained to show that the redistribution of the total masses of the proteins comprising the biochemical network is the key process underlying pattern forming dynamics. Based on the assumption that mass redistribution is indeed the key process, we inferred that the concerted action of two mutually commensurable modes q_c and $q_r = 2q_c$ is responsible for the transition from chemical turbulence to long range coherent standing wave order. Indeed, the point where the commensurable mode $q_r = 2q_c$ becomes linearly unstable marks the threshold where the phenomenology of the spatiotemporal dynamics changes on a qualitative as well as a quantitative level, gaining characteristic features set by the length scales l_c and l_r:

- The turbulent pattern becomes a standing wave pattern with wavelength approximately given by l_c.
- The change of local stability becomes spatially correlated and the corresponding cor-

relation length increases with the control parameter h.

- The correlation function of local stability change oscillates on a length scale set by l_c which sets the distance separating source/sink defects.

- The redistribution of total mass occurs on a length scale set by $l_r/2$. This controls the positions where wavefronts emitted by the source defects are formed (c.f. main text Fig. 4).

In addition the proposed mechanism based on mutually commensurable modes controlling local stability enabled us to infer the precursor dynamics close to the transition from turbulence to standing wave order. In particular, we were able to predict and explain:

- Standing waves trains propagating at a finite velocity $v_w \gtrsim \delta/\tau$ in different directions.

- Moving domain interfaces (with speed $v_I \lesssim l_c/\tau$) separating the direction of wave-node propagation.

- A preferred formation of propagating wave trains close to the interface in one domain and turbulent dynamics (phase slips defects) in the other domain closely below the transition (weak incommensurability).

- Bands of propagating wave packets that tend to maintain a constant distance between wave nodes thereby showing short to intermediate range coherence closely beyond the transition in the standing wave regime (weak commensurability).

Taken together this presents a large set of independent evidence that strongly supports the conclusion that the relevant part of the pattern forming dynamics in mass-conserved reaction-diffusion systems is the redistribution of total mass by unstable modes activated in a lateral instability. We therefore summarise that **order emerges from the control of local stability**.

X. THE TRANSITION TO LOCAL OSCILLATIONS AND SIMILARITIES BETWEEN THE MIN SYSTEM AND THE CO–PT SYSTEM

A. The local oscillatory instability is subcritical

To further investigate the local dynamics at the transition to local instability we consider an isolated cytosolic column, i.e. a one-dimensional column of length h (representing the bulk height) with reactive boundary conditions (Eq. 31a-31c) at $z=0$ and no-flux boundary conditions at $z=h$ (Eq. 32a-32c). The parameters are identical to those given in Table 1 (for the laterally extended system), therefore, the steady state coincides with the uniform steady state in the spatially extended system. As described in Supplementary Section IV, we perform a linear stability analysis of the steady state by setting $q = 0$ (the stability of

the membrane point is equivalent to the stability of the extended membrane against uniform perturbations represented by the zero mode ($q = 0$)). This reveals that the steady state of this system will become unstable for $h = h_{\mathrm{Loc}} \geq 36.3 \mu m$ (Supplementary Fig. 10B, c.f. main text Fig. 4b). To test this stability analyis we performed simulations of the one-dimensional system. First we used the computed steady states u_i^* as initial conditions (c.f. Section IV), and perturbed the bulk profiles (Eq. 61) spatially with white noise,

$$u_i(z, 0) = u_i^*(z) \ [1 + 0.02\Phi(z)] \ , \tag{101}$$

where $\Phi(z)$, at every point in space z, is drawn from a standard normal distribution (zero mean, and unit (1) variance). We kept the membrane densities unperturbed to minimise the perturbation of total mass (the bulk perturbation is zero on average, i.e. $\int_0^h \mathrm{d}z \ \Phi(z) \approx 0$). The simulations precisely confirmed the critical bulk height for the onset of autonomous oscillations, see Supplementary Fig. 10A. We also observed that the dynamics always enter a large amplitude limit cycle, regardless of the distance from the bifurcation at h_{Loc}. Since the amplitude does not vanish as the bifurcation is approached from above the bifurcation appears to be subcritical.

To consolidate the possible subcriticality of the bifurcation, we ran additional simulations for bulk heights below the bifurcation, $h < h_{\mathrm{Loc}}$, with initial conditions far from the steady state, specifically with all MinD on the membrane and all of MinE in the cytosol. Indeed, the simulations (Supplementary Fig. 10C) confirm that the large amplitude limit cycle exists before the steady state becomes unstable, and it can be reached for these particular initial conditions for $h \geq 35 \, \mu m$. Hence, the dynamics indeed show clear signs of excitability. It is worth pointing out that we did not find any stable limit cycles for $h = 33 \, \mu m$, i.e. the value where the spatially extended system undergoes a chimera transition from standing to travelling waves. Intuitively, one might have been inclined to ascribe the formation of the maintained source emitting travelling waves to the existence of a large amplitude limit cycle which is then reached by the pattern forming dynamics at the location of the source. Our results indicate that this limit cycle does not exist (or cannot be reached easily , i.e. has a small basin of attraction) for $h = 33 \, \mu m$ (and our choice of total densities of MinD and MinE) in the uniform state (which is equivalent to the point oscillator studied above). In turn, this implies that for the limit cycle to be created (made reachable) one has to change the total densities locally (here, by increasing the local MinE/MinD ratio Δ).

B. Are Min protein patterns *in-vitro* based on the same mechanism as patterns *in vivo*?

So far, Min protein patterns *in vivo* and *in-vitro* have been unanimously seen as an example for Turing patterns in a biological system. As a reminder for the reader: The mechanism for pattern formation found by Alan Turing, and now commonly referred to as Turing instability, is fundamentally based on the assumption that local dynamics (i.e. with lateral diffusion turned off) are in a stable chemical equilibrium. The astonishing discovery that

Alan Turing made was that (lateral) diffusive coupling of these locally stable dynamics can lead to an instability that induces the formation of a non-uniform pattern form an initially uniform state. This is surprising and highly counterintuitive because diffusion is supposed to remove any concentration gradients and not induce them. *In vivo*, the assumption of a Turing mechanism for the Min protein dynamics appears to be justified. Theoretical models [8, 10] have shown that there is a critical cell length for the onset of pattern formation below which the system is uniform and stable. Furthermore, in almost two decades of experimental research on Min protein dynamics there has been (to the best of our knowledge) not a single report of *blinking* cells, i.e. cells that show uniform oscillations without any spatial heterogeneity (of course, this would biologically be undesired). However, in the case of *in-vitro* patterns, our analysis suggests that the Min protein patterns as observed experimentally (travelling waves and spirals) actually originate from local oscillatory dynamics. Therefore, the Min system *in-vitro* represents an example for an oscillatory medium and not a Turing mechanism. In the classical literature on pattern formation [1, 2, 13], the field of oscillatory media is mostly seen as a class of pattern forming systems that are distinct from Turing systems. It is, therefore, particularly interesting that the Min proteins are able to generate patterns based on both mechanisms, only by a change of the system geometry (which is accompanied by a change of diffusion coefficients and total particle numbers). Investigating the transition between both mechanisms as control parameters are varied will be a very interesting future research project.

C. A mechanistic connection between the Min system and the CO–Pt system?

The heterogeneous catalysis of carbon monoxide oxidation (CO) on platinum (Pt) crystal lattices has been widely studied for its industrial application, and for its ability to form oscillatory patterns as spiral waves, standing waves, target patterns, and a broad range of irregular and chaotic wave phenomena [14–16]. At first glance, the structure of the reaction network appears to be very different from the Min system (and most other biological systems). Instead being based on the cycling between different states, the dynamics require a constant supply of CO and O_2 which is transferred into CO_2, without the reverse reaction taking place. However, the essential nonlinear process driving the CO oxidation is the catalytic action of the platinum lattice, which has a fixed and finite number of binding sites. The importance of this conservation law for the oscillatory dynamics has been nicely summarized by G. Eigenberger[17]:

> "The oscillation observed with the CO- and H_2-oxidation on platinum however often had the character of relaxation oscillations. This class of oscillations can be interpreted by the combination of one storage element with a switching device which changes the direction of the current to and from the storage."

Here storage denotes the dynamical reservoir of free binding sites, and the switching element the nonlinear kinetics selecting between predominant CO/O_2 adsorption and catalytic CO_2 desorption. It is important to note that this discussion addresses the (uniform/local) oscillation of the CO-Pt system, and not any aspect of pattern formation. To establish a clear conceptual connection to the *in-vitro* Min dynamics on the level of local oscillations, let us consider the dynamics of a point on the membrane in the oscillatory regime $h > h_{\mathrm{Loc}}$ (cf. main text Fig. 4b). In supplementary section VI A we have discussed that the calculation of the control variable (from which we infer local equilibria) is based on the adiabatic extrapolation of cytosolic protein densities near the membrane. This means, that only protein densities that participate in the nonlinear dynamics at time t contribute to the control variables; cytosolic densities far away from the membrane do not. We find that once the local equilibrium undergoes a oscillatory instability, the control variables become locally oscillatory and we can analyze the local oscillation in the control space framework (see Supp. Fig. 12). Note that this example emphasizes that the concept of local equilibrium refers to locality in space and time. Let us have a look at the trajectory of the local oscillation in its local control space. The trajectory is centered around the total mass in the system, i.e. as obtained from bulk integrations instead of adiabatic extrapolation. During the oscillation, mass is being shuffled to and from this cytosolic storage. Hence, we can therefore identify it as the storage in the sense of Eigenberger's interpretation. The amplitude in control space encodes the fraction of mass which is not adiabatically slaved to (does participate in) nonlinear dynamics at the membrane point. We can also identify three distinct regimes in control space along the Δ axis: For low Δ (MinD dominance) the cytosolic storage is full. The dynamics are driven by MinD/MinE accumulation on the membrane, which depletes the storage. For high Δ (MinE dominance) the storage is empty. The dynamics are driven by MinE-catalyzed detachment from the membrane, which refills the storage. In between these two regimes lies the domain of local instabilities, which we can interpret as a "switching device which changes the direction of the current to and from the storage." This control space picture reveals the interconnection between switching and storage: The position in control space, i.e. the momentary level of the storage, regulates the nonlinear dynamics to and from the storage. This highlights the major concept of our mass redistribution framework: The local dynamics (in space and time) are determined by the position of the control variables in control space.

There are several interesting conclusions to be drawn from the preceding discussion:

- The generalization of *in-vitro* Min protein dynamics within the mass redistribution framework strongly implies a fundamental mechanistic connection between the Min system and the CO-Pt system. This is particularly remarkable, as the connection only becomes evident through the realization that the Min system studied *in-vitro* is an oscillatory medium — in contrast to Min dynamics *in vivo* (cf. supplementary section X B). Note that this result also directly follows from the control space analysis, i.e. the characterization of local equilibria and their stability through control variable dynamics.

- The analysis of the local oscillation in its control space characterizes the local Min oscillation *in-vitro* as a relaxation oscillation in control space. The local oscillation is driven by the transfer of mass between the reactive membrane and a cytosolic storage (non-adiabatic bulk). On the one hand, this finding emphasizes that bulk dynamics must be explicitly considered in models of the *in-vitro* Min system (this question has been under considerable debate in the literature, see [18]). On the other hand, it suggests that the bulk coupling in the Min system mainly fulfils the role of a storage element, which is a generic part of relaxation oscillations as pointed out by Eigenberger [17]. Note that there is also coupling to a bulk (the gas phase) in the CO-Pt system. However, in contrast to the Min system the dynamics in the gas phase can be neglected. Instead the (slow) restructuring of the finite (conserved) number of lattice sites serves as the storage element in the CO-Pt system.

- The essential control space variable driving the local Min protein relaxation oscillation is the ratio Δ between MinE and MinD.

- Explicitly mass–conserved models of the CO-Pt system were, to the best of our knowledge, only studied in context of the uniform oscillation [16], but not in context of CO pattern formation. Our results show that Min protein dynamics are capable to generate very similar patterns as the CO-Pt system, including standing waves and spirals, as well as chemical turbulence. We explained these phenomena by lateral mass redistribution through unstable modes. This lateral mass redistribution requires different diffusion coefficients between the different components of a conserved species (cf. supplementary section I). In case of the CO-Pt system, the conserved species is the Pt lattice, its components are the occupation states (empty, CO occupied, O_2 occupied). Since CO is weakly bound to Pt (compared to O_2), it is usually considered as diffusing component in classical models (cf. [14]), while O_2 is considered to be immobile. Therefore, the generic prerequisites for lateral mass redistribution are given, and an analysis of mass conserved CO-Pt models in our control space framework could shed new light on the principles and conditions underlying CO pattern formation on Pt surfaces.

XI. SUPPLEMENTARY FIGURES

A. Supplementary Figure 1: Lateral instabilities in mass–conserving two–component systems

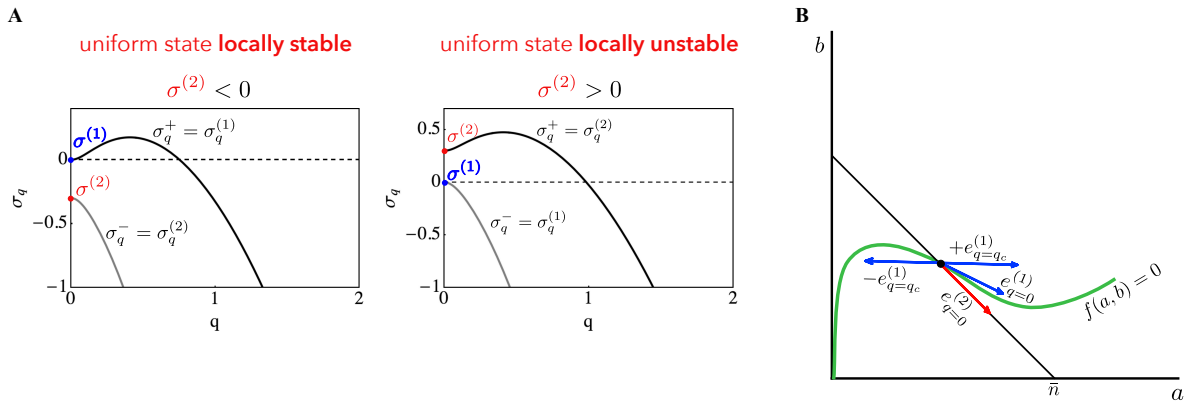

Supp. Fig. 1

A, Exemplary dispersion relations for the situation where the uniform state is locally stable ($\sigma^{(2)} < 0$) and the dispersion is governed by $\sigma_q^{(1)}$ (left), and the situation where the uniform state is locally unstable ($\sigma^{(2)} > 0$) such that this instability governs the dispersion relation. **B**, Phase-space illustration of the eigenvectors associated with unstable modes. The eigenvectors associated with uniform perturbations $q = 0$ parametrise the line of fixed points $e^{(1)}_{q=0}$ and the local phase space $e^{(2)}_{q=0}$respectively. The eigenvector of the fastest growing mode $e^{(1)}_{q=q_c}$ (assuming local stability, i.e. $\sigma^{(2)} < 0$) points away from the line of fixed points and from the local phase space of the uniform state $\bar{n}$, showing that the lateral instability induces a lateral redistribution of total density.

B. Supplementary Figure 2: Wave–pinning in the mass–redistribution framework

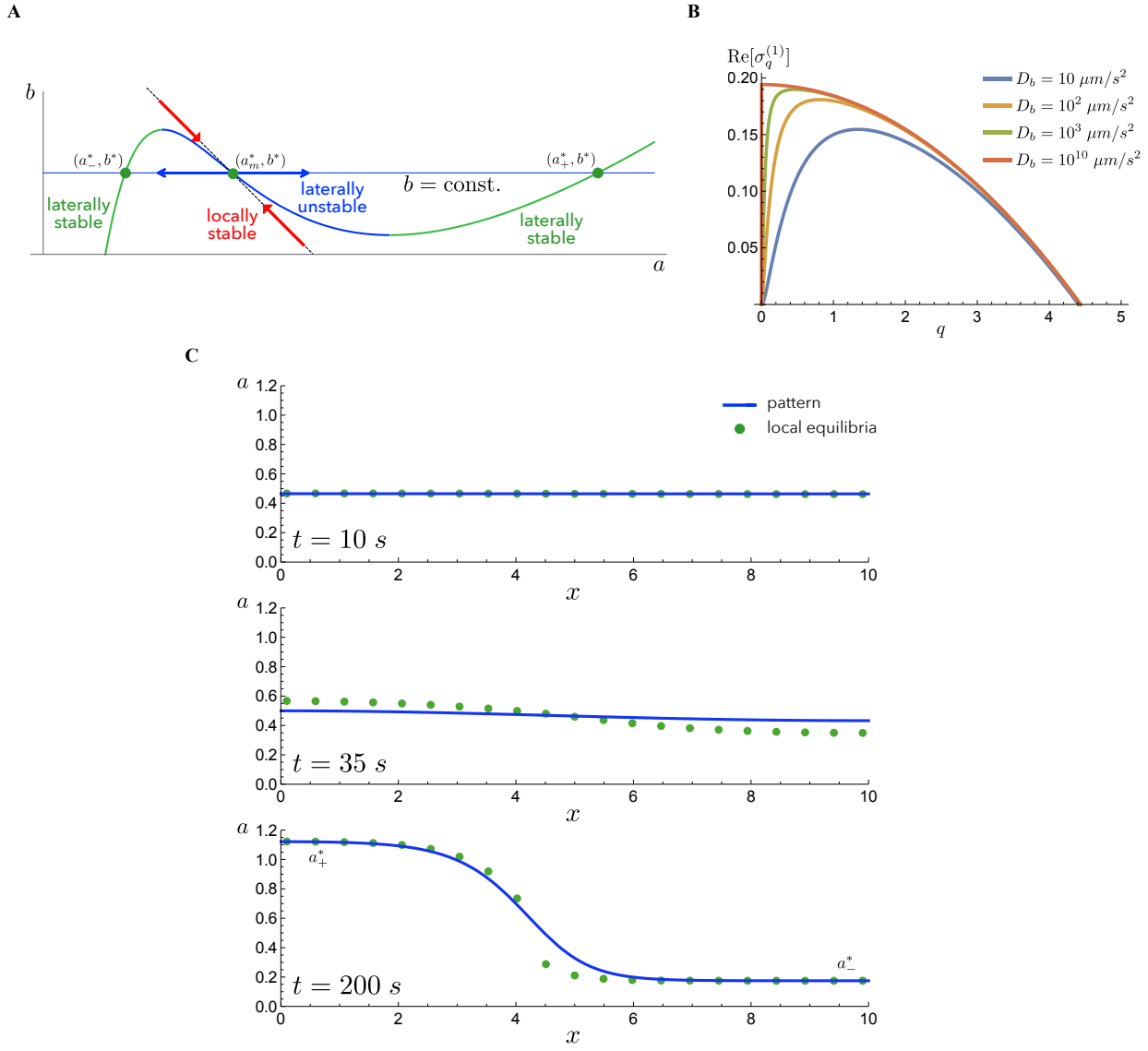

Supp. Fig. 2

A, Phase space illustration of the wave–pinning model (Eq. 18-20, cf. main text Fig 1b). For $D_b/D_a \gg 1$ ($D_b \to \infty$) the system is constrained to a subspace $b = \text{const.}$ (blue line). The curve shows the line of equilibria ($f(a, b) = 0$) and its intersections with the subspace of the pattern mark the local equilibria (a^*_-, b^*) and (a^*_+, b^*) used in the construction of the polarized state [3, 4]. The blue highlighted part of the nullcline marks the part where the uniform state is laterally unstable (Turing instability). The flow induced by the lateral instability is depicted by the blue arrows. **B**, Dispersion relations for the wave–pinning model (Eq. 18-20, $\bar{n} = 2.35$) for various cytosolic diffusion constants D_b. The data clearly shows that as $D_b \to \infty$ the fastest growing mode approaches the zero mode $q = 0$ but $q = 0$ remains marginally stable ($\sigma^{(1)}_{q=0} = 0$) for any finite D_b. **C**, Snapshots from the simulation of the wave–pinning model (Eq. 18-20, $\bar{n} = 2.35$) staring with a weakly perturbed

uniform steady state. It can be clearly seen that the lateral instability of the uniform state induces a dynamic displacement of local equilibria (green dots) which scaffold the spatiotemporal evolution of the observed pattern (here membrane species a). The final pattern ($t = 200\ s$) is a diffusive interface spanned between plateaus determined by the local equilibria a^*_- and a^*_+.

C. Supplementary Figure 3: Control space parametrization for the Min model

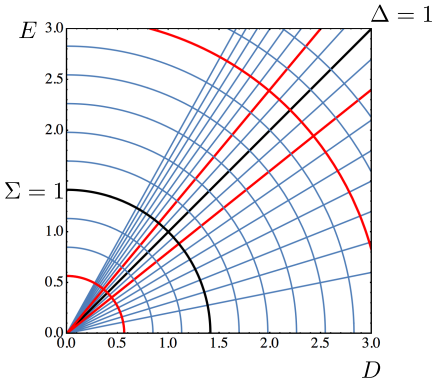

Supp. Fig. 3

For the Min model (cf. section III A) the control space is spanned by the (normalised) total densities of the conserved protein species MinD and MinE. With respect to this normalisation we consider coordinates given by the sum Σ and the ratio Δ of MinE and MinD. The highlighted area (red) shows the typical range in which the system is found in the simulations.

D. Supplementary Figure 4: Subcritical turbulence with cytosolic degradation

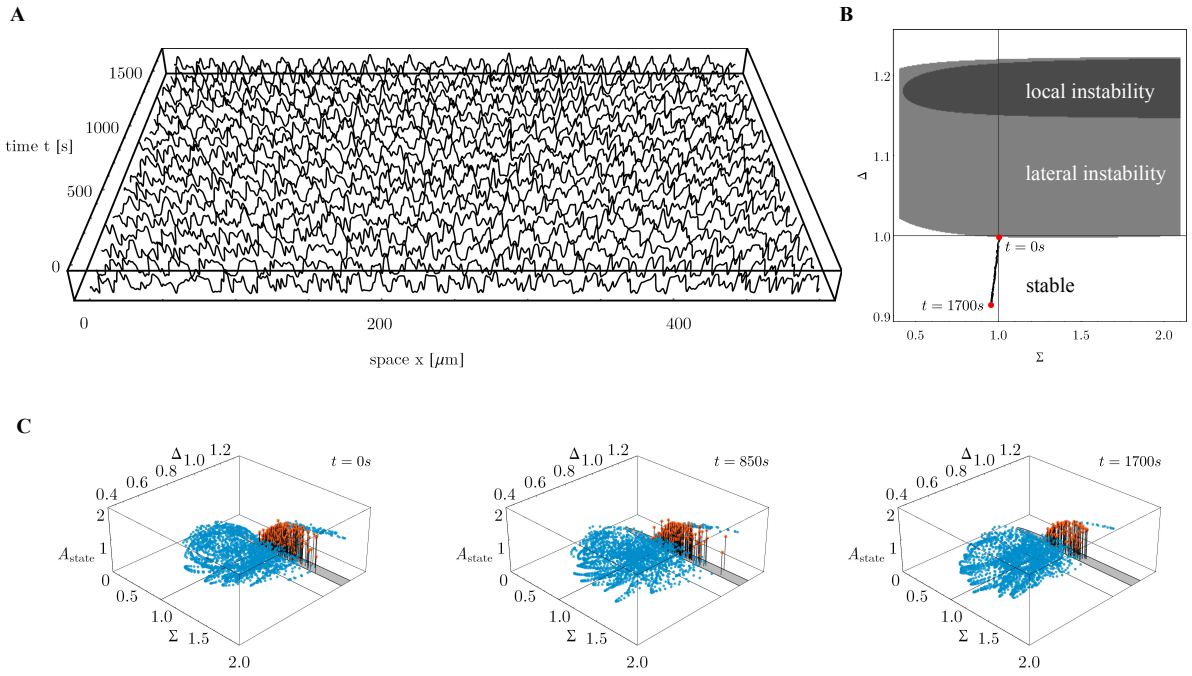

Supp. Fig. 4

Subcritical turbulence with cytosolic degradation. A, Wave profiles of the MinD densities on the membrane in the simulation with slow MinE degradation in the cytosol (see Supplementary Section VII). The data shows that the patterns is maintained even if the uniform state is stable. Hence, a lateral instability is not required to maintain chemical turbulence. **B**, Phase diagram of the control space showing the area where the uniform steady state is unstable laterally (light grey) and locally (dark grey). The line connecting the red dots shows the time evolution of the total densities as the system moves from the laterally unstable domain ($t = 0s$) into the stable domain ($t = 1700s$). **C**, Distribution of the system in control space (c.f. main text Fig. 3) as the system moves in the regime where the uniform state is stable. The data shows that the local dynamics keep entering and leaving the unstable domain, thereby maintaining chemical turbulence.

E. Supplementary Figure 5: Spatial correlation of local destabilisation

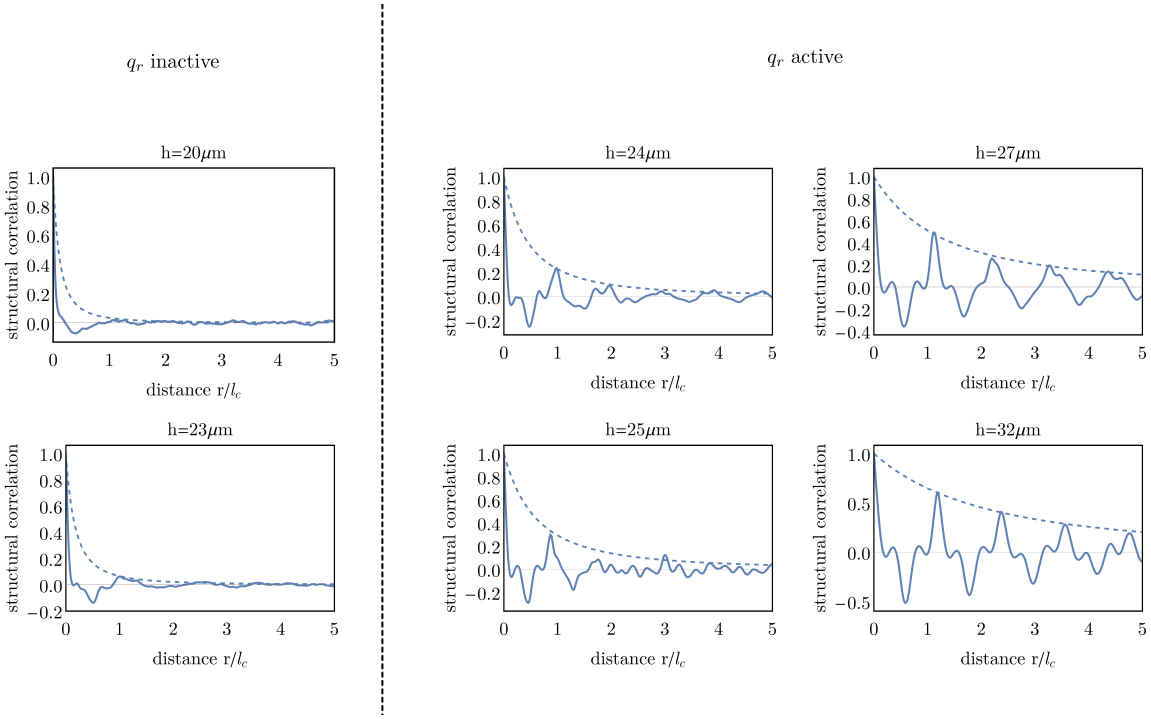

Supp. Fig. 5

Spatial correlation of local destabilisation. Table of spatial correlation functions $C(r/l_c)$ (blue solid lines) for different values of the system height (control parameter) h, indicated in the graph, with the corresponding envelopes $G(r/l_c)$ (dashed lines). The figure is split into two panels, one where the commensurable mode $q_r = 2q_c$ is inactive (stable) [left], and the other where it is active (unstable) [right]. The data shows that the spatial correlation oscillates with a period set by the fastest growing mode $q_c = 2\pi/l_c$ close to the transition.

F. Supplementary Figure 6: Correlation length dependence on mode commensurability

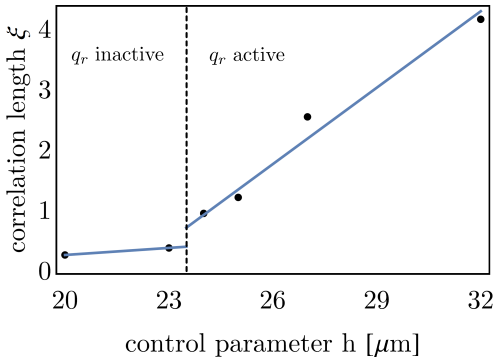

Supp. Fig. 6

Correlation length dependence on mode commensurability, The correlation length ξ as a function of the control parameter h extracted from the envelope fits $G(r/l_c) = ((r/l_c)/\xi + 1)^{-2}$ in Supp. Fig. 5. The data shows a clear transition at the value of the control parameter $h = 23.5\mu m$ where the commensurable mode $q_r = 2q_c$ becomes active. Beyond the transition the spatial correlation increases monotonously (linear fit included for convenience).

G. Supplementary Figure 7: Cluster distance distributions

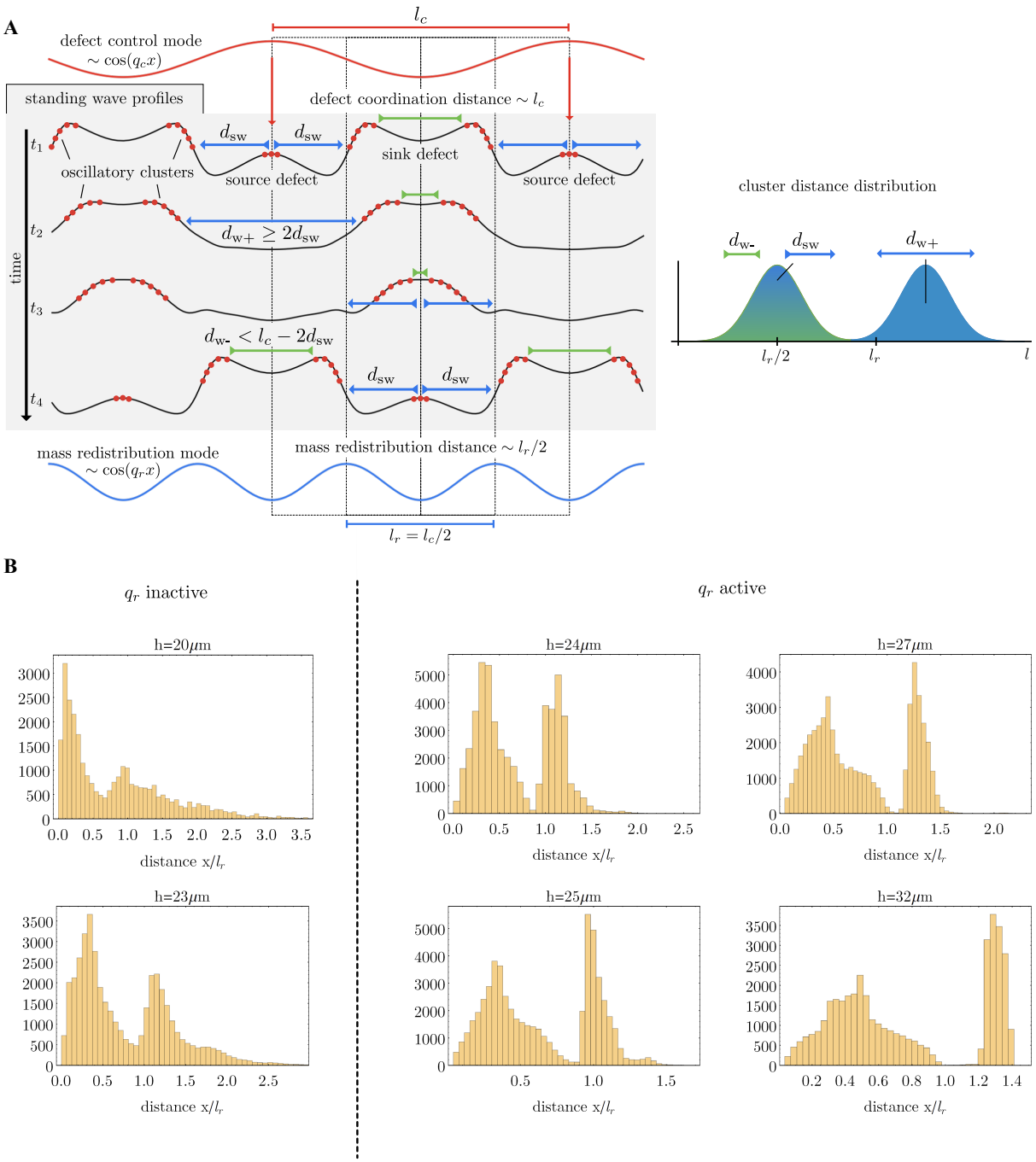

Supp. Fig. 7

Cluster distance distributions, **A**, Reprint of main text Figure 4d with the added definitions of cluster distance length scales d_{sw}, d_{w+}, and d_{w-}.

B, Histograms with the distance-distribution of local instability clusters for various values of the control parameter h. All distances are rescaled to the respective length scale set by the commensurable (mass redistribution) mode $q_r = 2\pi/l_r$.

The bimodal distribution shows a clear separation between both peaks for values of the control parameter $h > 23.5\mu m$ where the commensurable mode $q_r = 2q_c$ is active. In this regime the first peak aligns with the characteristic distance of mass redistribution $l_r/2$ mediated by the commensurable (mass redistribution) mode q_r, and the second peak becomes bound from below by l_r.

H. Supplementary Figure 8: Control mode alignment in the weakly incommensurable regime

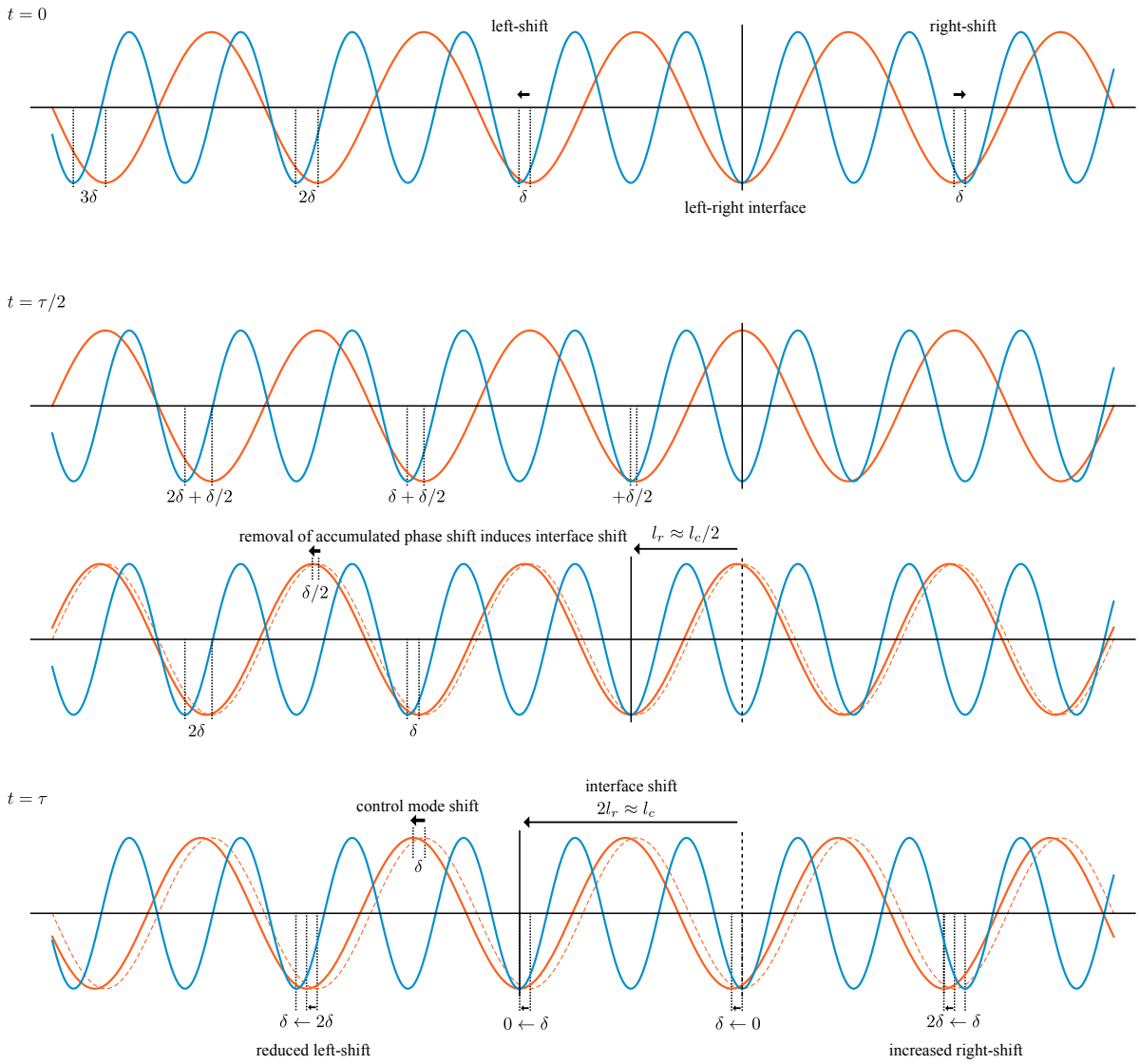

Supp. Fig. 8

Schematic of the precursor phenomenon, At $t = 0$ s we align the troughs of the weakly incommensurable control modes q_c (red) and $q_{\max}$ (blue) at some point in space. Right and left to this *interface* the weak incommensurability causes a phase shift of $+\delta$ and $-\delta$ of the mass redistribution mode ($q_{\max}$) with respect to the defect control mode (q_c), which increases by $\pm\delta$ with each wave node away from the interface. After a half temporal period this phase difference has increased by $\delta/2$ at each node to the right and the left, respectively. This increase increase can only be reduced by shifting the defect control mode q_c (the unshifted modes are plotted with dashing for reference). However, as illustrated for $t = \tau$, while this will decrease the phase shift at one side, it will increase the phase shift at the other side. It will also lead to movement of the interface by one spatial period per oscillation cycle, $v_I \approx l_c/\tau$.

I. Supplementary Figure 9: Point-to-point correlation kymographs

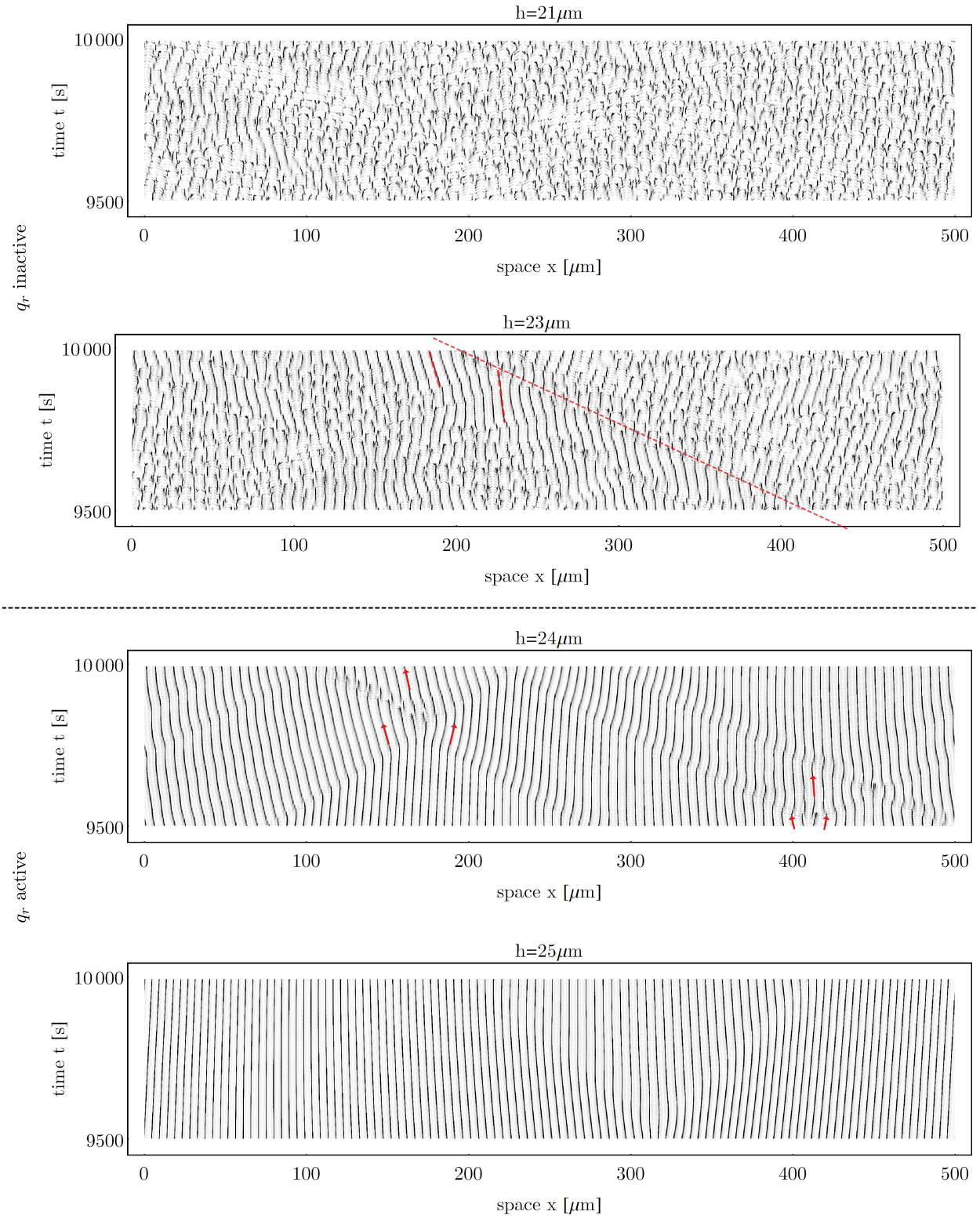

Supp. Fig. 9

Point-to-point correlation kymographs, The kymographs show the point-to-point correlation as defined in the Supplementary section VIII for increasing values of the control parameter h. The greyscale reflects the correlation of nearby membrane signals with light values corresponding to high correlation. We observe chemical turbulence in the regime where the commensurable mode q_r is inactive and the transition to standing wave patterns once q_r is activated (for $h > 23.5\mu m$). For $h = 23\mu m$ the mode with the smallest wavelength $q_{\max}$ is almost commensurable with the fastest growing mode q_c (phase difference $\delta/l_c = 0.03$, c.f. Supplementary section IX D). As expected we observe the formation of short bands of propagating wave trains (thick red lines) bounded by phase boundaries that separate predominant phase propagation direction (highlighted by the light red line).

J. Supplementary Figure 10: The Min point oscillator

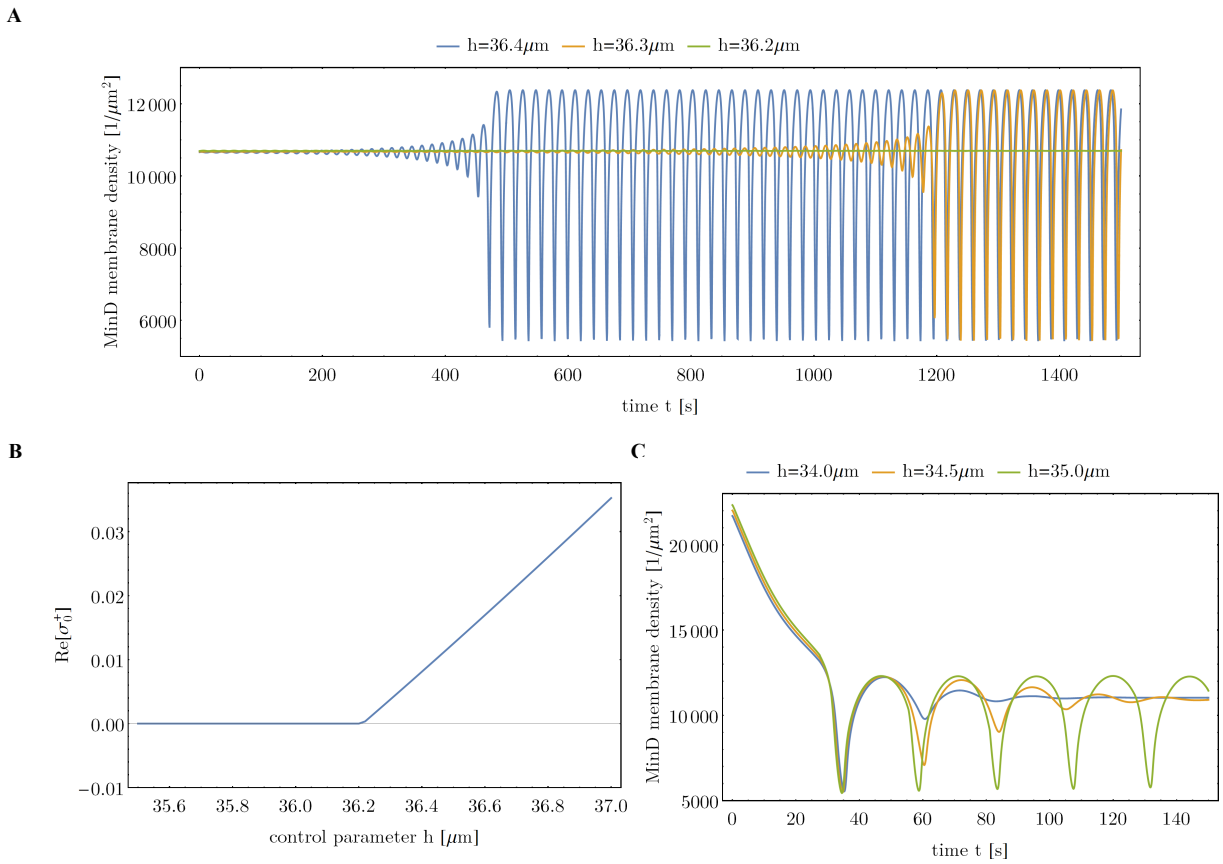

Supp. Fig. 10

The Min point oscillator. A, Time evolution of membrane bound MinD ($u_d + u_{de}$) in a one dimensional system (bulk column with reactive boundary as membrane) starting with a initial condition in the vicinity of the steady state. The data show exponential growth for $h > 36.2\mu m$ as expected from the stability analysis in **B**. **B**, The growth rate $\mathrm{Re}[\sigma_0^+]$ shows the stability of the uniform steady state against uniform perturbations (in this case reflecting the stability of steady state in the 1 dimensional bulk column). **C** Time evolution of membrane bound MinD ($u_d + u_{de}$) in a one dimensional system (bulk column with reactive boundary as membrane) starting with an initial condition where MinD is on the membrane and MinE is in the cytosol. The data shows stable limit cycles even if the equilibrium of the system is stable.

K. Supplementary Figure 11: Supplementary data

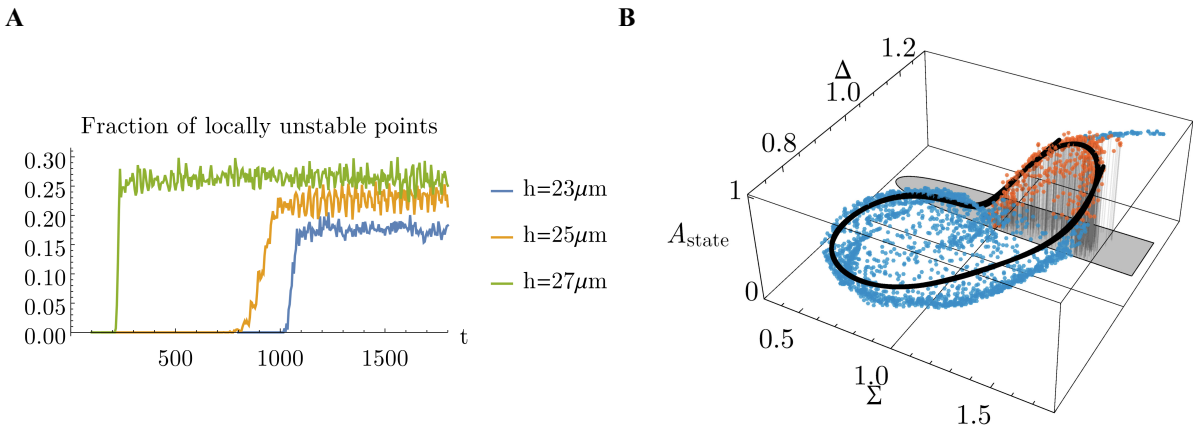

Supp. Fig. 11

Supplementary data. **A**, Fraction of locally unstable equilibria extracted from simulation for increasing values of the control parameter h. The fraction of local instabilities increases with h and local destabilisation occurs sooner as the regime of local instability approaches the global average in control space (c.f. main text Fig. 2d and 4b). **B**, Distribution of the whole system in control space (Σ, Δ) and corresponding distances to local equilibria $A_{\text{state}}(x,t)$ (c.f. main text Fig. 3a) for $h = 25\mu m$ at $t = 625s$. With the onset of finite spatial correlation the distribution starts to contract towards a circle in control space (Σ, Δ). A single trajectory for a fixed spatial position ($x = 28\mu m$, $t = 600 \ldots 650s$) is highlighted in black.

L. Supplementary Figure 12: The local Min oscillation *in-vitro* in control space - an analogy to the CO-Pt relaxation oscillator

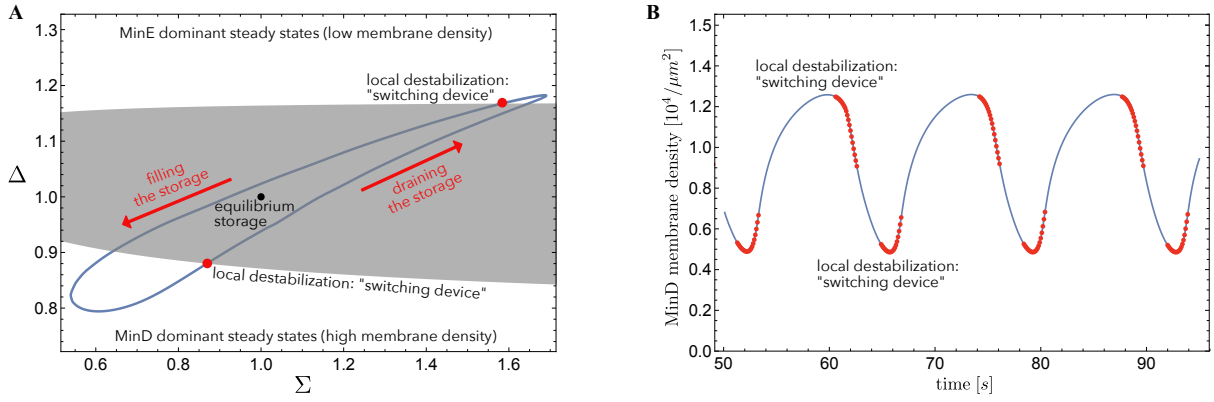

Supp. Fig. 12

The local Min oscillation *in-vitro* in control space. A, The trajectory of an laterally isolated point (cf. Supp. Fig. 10) in control space ($h = 60\mu m$). The local equilibria are computed using the adiabatic extrapolation of the bulk state (cf. section VI A). The point $(1, 1)$ represents the average total density in the system. The data shows that the oscillation can be identified as a relaxation oscillation comprising a storage element and a switching device as heuristically described by G. Eigenberger for the CO-Pt system [17]. In the MinD and MinE dominant regimes the system approaches stable local equilibria with high and low membrane densities respectively. These regimes correspond to distinct values of the control variables. The dynamics of the control variables represent the periodic filling and draining of the cytosolic storage. The local destabilization acts as a "switching device" between draining and filling this storage. Hence, the non-adiabatic cytosol in the Min system has a similar role as the delayed restructuring of the platinum lattice in the CO-Pt system. **B**, The local oscillation of the MinD membrane densities for the data in Supp. Fig. 10A. The blue parts represent the sections of the trajectory where the local equilibria are stable. Local destabilization acts as switch (in the sense of Eigenberger) between accumulation and depletion of the membrane.

XII. MOVIE CAPTIONS

A. Movie 1: Onset of chemical turbulence

Top: Membrane profile of MinD during the transition from small amplitude standing waves to chemical turbulence for a control parameter (bulk height) $h = 20\mu m$. (Also, see main text Fig. 3b)

Bottom: Temporal evolution of the system's distribution in control space corresponding to the time step shown in the top wave profiles. (Also, see main text Fig. 3a)

B. Movie 2: Emergence of standing wave order

Top: Membrane profile of MinD at the onset of standing wave order for a control parameter (bulk height) $h = 25\mu m$. (Also, see main text Fig. 4c)

Bottom: Temporal evolution of the system's distribution in control space corresponding to the time step shown in the top wave profiles. (Also, see Supplementary Fig. 11B)

C. Movie 3: Spiral wave patterns in a 3d box geometry

Spatiotemporal dynamics of membrane bound MinD in the simulation of the full 3d box geometry for a control parameter (bulk height) $h = 100\mu m$.

D. Movie 4: Chimera transition from standing to travelling waves

Top: Membrane profile of MinD during the chimera transition from from standing to travelling waves (light grey highlighted area) for a control parameter (bulk height) $h = 33\mu m$. (Also, see main text Fig. 5b)

Bottom: Temporal evolution of the system's distribution in control space corresponding to the time step shown in the top wave profiles. (Also, see main text Fig. 5e) Data points corresponding to the spatial domain in the grey highlighted area (in the top wave profile) are plotted opaque to show the contraction of the distribution in control space to a well

defined cycle.

---

[1] M. Cross and H. Greenside, *Pattern Formation and Dynamics in Nonequilibrium Systems* (Cambridge University Press, 2009).

[2] M. Cross and P. Hohenberg, Reviews of modern physics **65** (1993).

[3] Y. Mori, A. Jilkine, and L. Edelstein-Keshet, Biophysical journal **94**, 3684 (2008).

[4] Y. Mori, A. Jilkine, and L. Edelstein-Keshet, SIAM Journal on Applied Mathematics **71**, 1401 (2011).

[5] A. B. Goryachev and M. Leda, Molecular Biology of the Cell **28**, 370 (2017).

[6] P. K. Trong, E. M. Nicola, N. W. Goehring, K. V. Kumar, and S. W. Grill, New Journal of Physics **16** (2014).

[7] K. C. Huang, Y. Meir, and N. S. Wingreen, Proceedings of the National Academy of Sciences of the United States of America **100**, 12724 (2003).

[8] J. Halatek and E. Frey, Cell reports **1**, 741 (2012).

[9] F. Wu, B. G. C. van Schie, J. E. Keymer, and C. Dekker, Nature Nanotechnology (2015).

[10] F. Wu, J. Halatek, M. Reiter, E. Kingma, E. Frey, and C. Dekker, Molecular Systems Biology **12**, 642 (2016).

[11] M. Loose, E. Fischer-Friedrich, J. Ries, K. Kruse, and P. Schwille, Science (New York, N.Y.) **320**, 789 (2008).

[12] Remark: Since $q_{\max}$ has zero growth rate mass redistribution will be mediated by a mode $q \lessapprox q_{\max}$). for simplicity we will still refer to the mode as $q_{\max}$.

[13] Y. Kuramoto, *Chemical Oscillations, Waves and Turbulence* (Springer, Berlin, 1984).

[14] A. S. Mikhailov and K. Showalter, Physics Reports **425**, 79 (2006).

[15] M. Kim, M. Bertram, M. Pollmann, a. von Oertzen, a. S. Mikhailov, H. H. Rotermund, and G. Ertl, Science (New York, N.Y.) **292**, 1357 (2001).

[16] G. Eigenberger, Chemical Engineering Science **33**, 1263 (1978).

[17] G. Eigenberger, Chemical Engineering Science **33**, 1263 (1978).

[18] J. Halatek and E. Frey, Proceedings of the National Academy of Sciences **111** (2014), 10.1073/pnas.1220971111.